Aerospace Science and Technology 158 (2025) 109785

Contents lists available at ScienceDirect

Aerospace Science and Technology

journal homepage: www.elsevier.com/locate/aescte

Nonlinear dynamic analysis of the FG-TPMS double-curved panels: Introducing SVM-DNN-RF algorithm to predict nonlinear dynamic information

Shaoyong Han [a,b], Zhen Wang [c,d,*], Mohammed El-Meligy [e,f], Khalid A. Alnowibet [g]

[a] School of Mathematics and Computer Science, Tongling University, Tongling, Anhui 244061, PR China
[b] Anhui Tongguan Intelligent Technology Co., Ltd., Tongling, Anhui 244000, PR China
[c] School of Data Science and Artificial Intelligence, Wenzhou University of Technology, Wenzhou, Zhejiang 325035, PR China
[d] Faculty of Computing, Universiti Teknologi Malaysia, Johor Bahru, Johor 81310, Malaysia
[e] Jadara University Research Center, Jadara University PO Box 733, Irbid, Jordan
[f] Applied Science Research Center, Applied Science Private University, Amman, Jordan
[g] Statistics and Operations Research Department, College of Science, King Saud University, Riyadh 11451, Kingdom of Saudi Arabia

ARTICLE INFO

Editor:Jang-Kyo KIM

Keywords:
Nonlinear dynamics
SVM-DNN-RF algorithm
FG-TPMS
Doubly curved panel
External excitation

ABSTRACT

This study presents a nonlinear dynamic analysis of functionally graded (FG) Triply Periodic Minimal Surface (TPMS) double-curved panels under various excitation conditions. The TPMS structures, characterized by their complex geometry and favorable strength-to-weight ratio, are increasingly used in advanced engineering applications. Using time-domain and phase-space analysis, the influence of structural parameters and excitation frequencies on the transverse displacement and velocity responses of the FG-TPMS panels was examined. Results reveal that modifications in the excitation frequency significantly affect the panels' vibrational behavior, leading to complex oscillatory patterns and nonlinear phase trajectories. This study introduces the SVM-DNN-RF algorithm, a hybrid model combining Support Vector Machine (SVM), Deep Neural Network (DNN), and Random Forest (RF) techniques to predict nonlinear dynamic behaviors from mathematically simulated datasets. By leveraging the strengths of each model—SVM's classification accuracy, DNN's deep feature extraction, and RF's robustness—the proposed algorithm achieves high predictive accuracy and generalization in capturing complex nonlinear dynamics. Results demonstrate that SVM-DNN-RF effectively handles nonlinear relationships and improves predictive performance compared to standalone models. This approach offers a powerful tool for applications requiring precise dynamic analysis, such as structural engineering, physics simulations, and complex system modeling. This complexity highlights the sensitivity of FG-TPMS panels to design and operational parameters, providing insight into optimizing these structures for improved resonance control and damping in applications requiring lightweight yet strong materials. These findings contribute to the design of advanced structural systems with tailored dynamic properties.

1. Introduction

Functionally graded materials (FGMs) are becoming increasingly important in the field of engineering due to their unique properties that offer significant advantages over conventional materials [1]. These materials are characterized by a gradual variation in composition and structure, which allows for tailored performance across different regions of a component. FGMs are particularly valuable in applications that require specific mechanical, thermal, or chemical properties in different parts of a structure, such as in aerospace, automotive, and biomedical engineering [2]. One of the key benefits of FGMs is their ability to provide improved thermal resistance, making them ideal for environments with extreme temperature gradients, such as turbine blades or heat shields [3,4]. Engineers can design functionally graded structures that optimize the distribution of materials, combining the strengths of each phase to achieve superior overall performance [5]. For instance, an FGM can have a high-strength material on one side for mechanical load-bearing and a more heat-resistant material on the other side for

* Corresponding author.
E-mail address: wangzhen@wzu.edu.cn (Z. Wang).

https://doi.org/10.1016/j.ast.2024.109785
Received 29 August 2024; Received in revised form 13 November 2024; Accepted 27 November 2024
Available online 5 December 2024

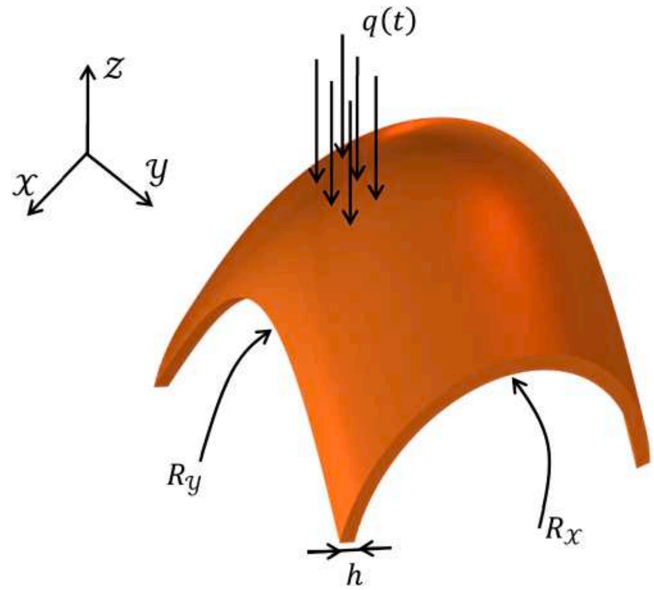

Fig. 1. A real schematic view and geometry of the curved panel and curved panel made of TPMSM under frequency excitation.

thermal protection, without the need for joints or interfaces that could fail under stress [6]. The ability to fine-tune material properties in this way helps reduce the risk of failure and increases the efficiency of the component [7]. Additionally, FGMs often exhibit superior wear and corrosion resistance, reducing maintenance costs and increasing the service life of critical parts in harsh environments [8]. The flexibility of FGMs extends to their ability to reduce the weight of components while maintaining high performance, which is crucial in industries such as aerospace and automotive, where weight reduction leads to improved fuel efficiency [9]. Functionally graded materials also enable the creation of complex geometries that are difficult to achieve with traditional manufacturing methods [10]. Advances in additive manufacturing and processing technologies have further enhanced the feasibility of producing FGMs, enabling engineers to create highly customized components with intricate material gradients [11]. By using FGMs, engineers can achieve a balance between cost-effectiveness, performance, and sustainability [12]. The capability to tailor properties such as electrical conductivity, thermal expansion, and hardness makes FGMs an invaluable tool in designing next-generation materials for high-performance engineering applications [13]. As the demand for innovative, efficient, and environmentally friendly solutions continues to rise, functionally graded structures are poised to play a central role in shaping the future of engineering [14].

Functionally graded (FG) Triply Periodic Minimal Surface (TPMS) structures are increasingly valuable in engineering due to their unique combination of strength, lightweight design, and complex geometry [15]. These structures, which feature smooth, continuous surfaces with minimal material use, offer an excellent strength-to-weight ratio, making them ideal for applications where both durability and low mass are critical. Engineers are particularly drawn to FG-TPMS structures for their ability to withstand varied mechanical loads and resist deformation, enhancing the longevity and performance of structures [16]. The functionally graded aspect allows for tailored material properties, with gradual variations in composition or density, enabling precise control over stiffness, thermal resistance, and other mechanical characteristics [17]. This adaptability is highly beneficial in industries such as aerospace, automotive, and biomedical, where materials are exposed to demanding operational conditions [18]. Furthermore, the complex geometry of TPMS structures supports advanced energy absorption and damping properties, critical for vibration control [19]. Consequently, FG-TPMS structures provide engineers with innovative solutions for designing resilient, efficient, and customizable components across diverse engineering applications [20].

Nonlinear dynamics play a critical role in engineering, especially in systems where large deformations, complex material behavior, or significant changes in loading conditions occur [21]. Unlike linear systems, nonlinear dynamic responses are often sensitive to initial conditions, leading to complex behaviors like chaos, bifurcations, and resonance, which engineers must understand to ensure reliability and stability [22]. This complexity is particularly important in fields such as aerospace, mechanical, and civil engineering, where structures and materials are subject to unpredictable forces and environmental conditions [23].

Nonlinear dynamics provide insights into how systems respond under extreme or variable loads, helping engineers predict potential failure modes and optimize designs for resilience [24]. Understanding these dynamics also allows engineers to develop advanced damping and control mechanisms, crucial for reducing vibrations and enhancing performance in sensitive applications [25]. Additionally, nonlinear analysis enables the design of structures that are not only strong but also lightweight and efficient, meeting the increasing demand for sustainable solutions [26]. Overall, mastering nonlinear dynamics is essential for engineers aiming to innovate and improve safety, durability, and efficiency in complex systems [27]. As well as this, topology optimization of mechanical structures involves the computational design of material layout within a given space to maximize performance metrics like stiffness, strength, or weight efficiency under specific constraints [28]. By optimizing the distribution of material, engineers can create innovative, lightweight structures with enhanced mechanical properties tailored to withstand applied loads while reducing material usage [29].

Temperature-dependent material properties are crucial for accurate engineering design and performance prediction, as materials often exhibit varying mechanical, thermal, and electrical behaviors at different temperatures [30]. Understanding how properties such as strength, elasticity, and conductivity change with temperature ensures that structures and components can function reliably in extreme environments, preventing failures due to thermal stresses [31]. Incorporating temperature-dependent properties into designs allows engineers to optimize materials for efficiency, durability, and safety across a wide range of operating conditions [32].

In this work, functionally graded FG-TPMS double-curved panels are subjected to a nonlinear dynamic analysis under different excitation circumstances. Advanced engineering applications are using TPMS structures more and more because of their complicated geometry and advantageous strength-to-weight ratio. The effects of stimulation frequencies and structural characteristics (such as the b/a ratio) on the transverse displacement and velocity responses of the FG-TPMS panels were investigated using time-domain and phase-space analysis. The vibrational behavior of the panels is shown to be greatly impacted by changes in the b/a ratio and excitation frequency, resulting in complex oscillatory patterns and nonlinear phase trajectories. In order to forecast nonlinear dynamic behaviors from mathematically generated datasets, this paper presents the SVM-DNN-RF method, a hybrid model that combines SVM, DNN, and RF approaches. The suggested technique achieves excellent prediction accuracy and generalization in capturing complicated nonlinear dynamics by using the advantages of each model, including the resilience of RF, the deep feature extraction of DNN, and the classification accuracy of SVM. In comparison to solo models, the results show that SVM-DNN-RF enhances predictive performance and manages nonlinear interactions well. For applications like complex system modeling, physics simulations, and structural engineering that need accurate dynamic analysis, this method provides a potent tool. This study draws attention to how sensitive FG-TPMS panels are to operational and design factors, offering guidance on how to best optimize these structures for better damping and resonance control in applications that need robust but lightweight materials. These discoveries aid in the development of sophisticated structural systems with specific dynamic characteristics.

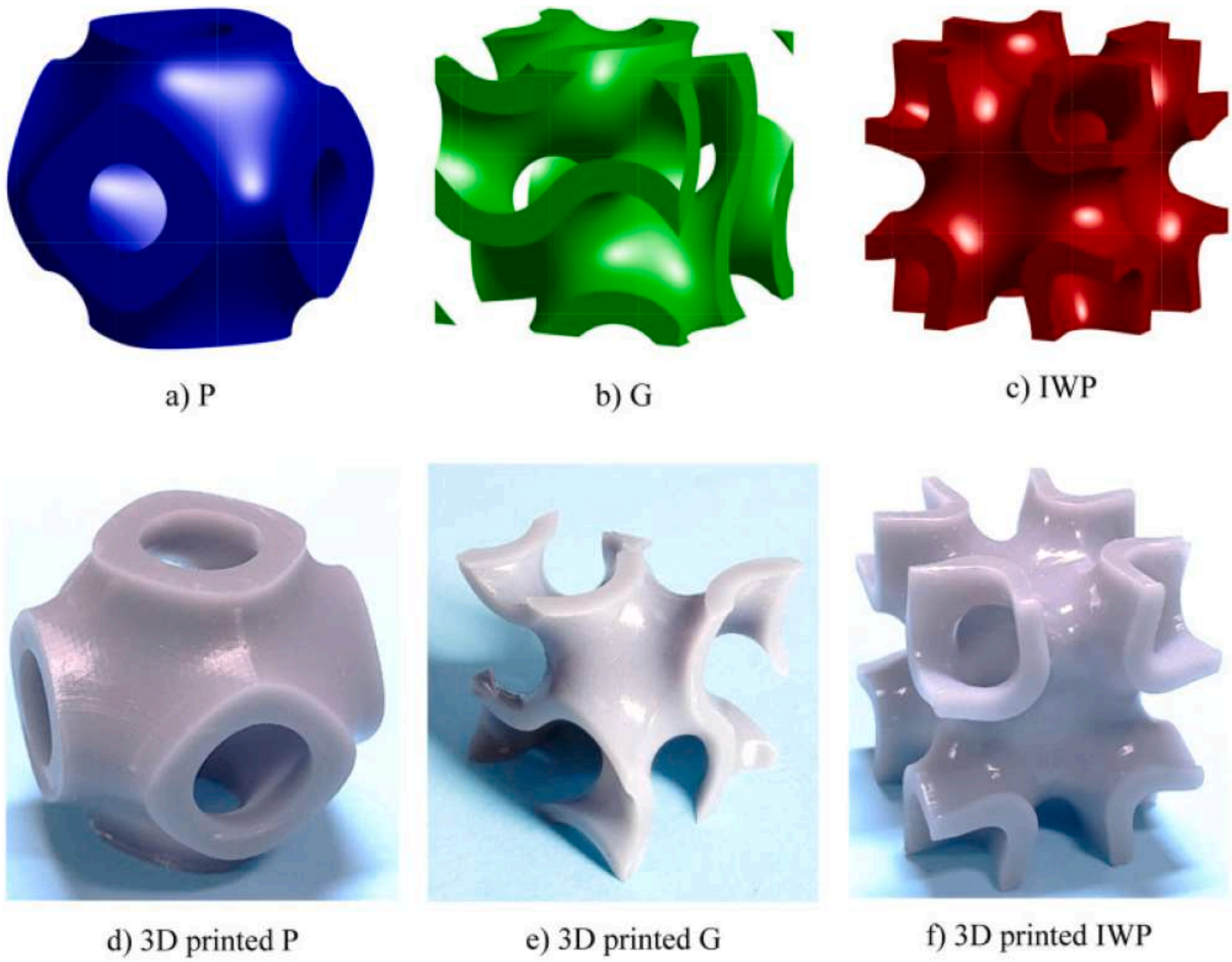

Fig. 2. An illustration of TPMS through the thickness of FG-TPMS double curved panels [34].

2. Mathematical modeling

Fig. 1 shows a schematic of a doubly curved panel made from a material identified as TPMSM, subjected to a time-dependent force $F(t)$. The geometry of the panel is defined by two radii of curvature, $R_{\mathscr{X}}$ and $R_{\mathscr{Y}}$ in the $\mathscr{X}$ and $\mathscr{Y}$ directions, respectively, and a thickness h. The force $q(t)$ acts perpendicularly to the surface, potentially inducing vibrations or deformations depending on the frequency of excitation. The three-dimensional coordinate system ($\mathscr{X}, \mathscr{Y}, \mathscr{Z}$) provides orientation, with the $\mathscr{X}$ and $\mathscr{Y}$ directions lying in the plane of the panel, and the z-axis perpendicular to it. This illustration likely supports a study on the dynamic response or vibrational characteristics of the curved panel structure under varying load conditions.

We investigate the geometrically nonlinear behaviors of functionally graded sheet-based TPMS plates in the present study. These sheet-based structures include three forms of TPMS: I-graph and wrapped package-graph (IWP), Primitive (P), and Gyroid (G). In general, the following equations [15] may be used to represent implicit mathematical functions that define these TPMS structures.

$$\text{Primitive}: \ \phi(\mathscr{X},\mathscr{Y},\mathscr{Z}) = \cos(\omega_{\mathscr{X}}\mathscr{X}) + \cos(\omega_{\mathscr{Y}}\mathscr{Y}) + \cos(\omega_{\mathscr{Z}}\mathscr{Z}), \tag{1a}$$

$$\begin{aligned}\text{Gyroid}: \ \phi(\mathscr{X},\mathscr{Y},\mathscr{Z}) &= \sin(\omega_{\mathscr{X}}\mathscr{X})\cos(\omega_{\mathscr{Y}}\mathscr{Y}) + \sin(\omega_{\mathscr{Y}}\mathscr{Y})\cos(\omega_{\mathscr{Z}}\mathscr{Z}) \\ &\quad + \sin(\omega_{\mathscr{Z}}\mathscr{Z})\cos(\omega_{\mathscr{X}}\mathscr{X}),\end{aligned} \tag{1b}$$

$$\text{IWP}: \ \phi(\mathscr{X},\mathscr{Y},\mathscr{Z}) = 2(\cos(\omega_{\mathscr{X}}\mathscr{X})\cos(\omega_{\mathscr{Y}}\mathscr{Y}) + \cos(\omega_{\mathscr{Y}}\mathscr{Y})\cos(\omega_{\mathscr{Z}}\mathscr{Z}) + \cos(\omega_{\mathscr{Z}}\mathscr{Z})\cos(\omega_{\mathscr{X}}\mathscr{X})) - (\cos(2\omega_{\mathscr{X}}\mathscr{X}) + \cos(2\omega_{\mathscr{Y}}\mathscr{Y}) + \cos(2\omega_{\mathscr{Z}}\mathscr{Z})). \tag{1c}$$

where ω_i indicates cyclic repeats of the TPMS cells, which are specified as follows; $\mathscr{X}$, $\mathscr{Y}$ and $\mathscr{Z}$ are the spatial coordinates of an arbitrary location.

$$\omega_i = \frac{2\pi n_i}{l_i}, \text{ with } i = \mathscr{X}, \mathscr{Y}, \mathscr{Z} \tag{2}$$

where n_i and l_i stand for the number of unit cells and TPMS structure lengths along the relevant axes, respectively. The following statement may be used to specify the architecture of sheet-based TPMS structures [33].

Table 1
Six density distribution cases with the same average value of 0.35.

Pattern	Case	ρ_{min}	ρ_{max}	n_A or n_B
A	A1	0.20	0.5	1.0
	A2	0.20	0.8	3.0
	A3	0.25	1.0	6.5
B	B1	0.20	0.5	0.561
	B2	0.20	0.8	1.757
	B3	0.25	1.0	3.943

$$-c \le \phi(\mathscr{X}, \mathscr{Y}, \mathscr{Z}) \le +c, \tag{3}$$

where c is the TPMS architecture control parameter. The volume of the TPMS unit may be easily changed by changing this parameter. In this study, we may get a uniform TPMS unit by setting the periodicity parameter for each of the three directions to the same value, such that $\omega_{\mathscr{X}} = \omega_{\mathscr{Y}} = \omega_{\mathscr{Z}} = \omega$. $\vartheta = l_{\mathscr{X}}/n_{\mathscr{X}} = l_{\mathscr{Y}}/n_{\mathscr{Y}} = l_{\mathscr{Z}}/n_{\mathscr{Z}}$ is the unit size of a TPMS architecture, as a consequence. Next, we may calculate this uniform unit's relative density (ρ) by

$$\rho = \frac{V}{\vartheta^3}, \tag{4}$$

where V is the volume of a sheet-based unit and ϑ^3 is its surrounding cube's volume.

2.1. Modeling of triply periodic minimal surface

In this study, we investigate three TPMS designs (Fig. 2) that pertain to the substrate layer structures: Primitive (P), Gyroid (G), and I-graph and Wrapped Package-graph (IWP) kinds.

Assume that the constitutive material of the shallow SS is functionally graded triply periodic minimal surface (FG-TPMS). Depending on the sheet-based architecture, three TPMS types are considered including Primitive type (P), Gyroid type (G), and I-graph and Wrapped Package-graph type (IWP) (see Fig. 2). In this paper, the effective properties such as the elastic modulus $E(\mathscr{Z})$, shear modulus $G(\mathscr{Z})$, and Poisson's ratio $\nu(\mathscr{Z})$ are determined according to the previous work [15] as follows:

- For type of Primitive (P)

$$E(\mathscr{Z}) = \begin{cases} E_s\left(0.317D_0^{1.264}\right) \; for \; D_0 \le 0.25 \\ E_s\left(1.007D_0^{2.006} - 0.007\right) \; for \; D_0 > 0.25 \end{cases}, \tag{5a}$$

$$G(\mathscr{Z}) = \begin{cases} G_s\left(0.705D_0^{1.189}\right) \; for \; D_0 \le 0.25, \\ G_s\left(0.953D_0^{1.715} + 0.047\right) \; for \; D_0 > 0.25 \end{cases}, \tag{5b}$$

$$\nu(\mathscr{Z}) = \begin{cases} 0.314e^{-1.004D_0} + 0.119 \; for \; D_0 \le 0.55, \\ 0.152D_0^2 - 0.235D_0 + 0.383 \; for \; D_0 > 0.55 \end{cases}, \tag{5c}$$

- For type of Gyroid (G)

$$E(\mathscr{Z}) = \begin{cases} E_s\left(0.596D_0^{1.467}\right) \; for \; D_0 \le 0.45, \\ E_s\left(0.962D_0^{2.351} + 0.038\right) \; for \; D_0 > 0.45 \end{cases}, \tag{6a}$$

$$G(\mathscr{Z}) = \begin{cases} G_s\left(0.777D_0^{1.544}\right) \; for \; D_0 \le 0.45, \\ G_s\left(0.973D_0^{1.982} + 0.027\right) \; for \; D_0 > 0.45 \end{cases}, \tag{6b}$$

$$\nu(\mathscr{Z}) = \begin{cases} 0.192e^{-1.349D_0} + 0.202 \; for \; D_0 \le 0.50, \\ 0.402D_0^2 - 0.603D_0 + 0.501 \; for \; D_0 > 0.50 \end{cases}, \tag{6c}$$

- For type of I-graph and Wrapped Package-graph (IWP)

$$E(\mathscr{Z}) = \begin{cases} E_s\left(0.597D_0^{1.225}\right) \; for \; D_0 \le 0.35, \\ E_s\left(0.987D_0^{1.782} + 0.013\right) \; for \; D_0 > 0.35 \end{cases}, \tag{7a}$$

$$G(\mathscr{Z}) = \begin{cases} G_s\left(0.529D_0^{1.287}\right) \; for \; D_0 \le 0.35, \\ G_s\left(0.960D_0^{2.188} + 0.040\right) \; for \; D_0 > 0.35 \end{cases}, \tag{7b}$$

$$\nu(\mathscr{Z}) = \begin{cases} 2.597e^{-0.157D_0} - 2.244 \; for \; D_0 \le 0.13, \\ 0.201D_0^2 - 0.227D_0 + 0.326 \; for \; D_0 > 0.13 \end{cases}. \tag{7c}$$

In the above expressions, E_s, G_s, and ν_s indicate the elastic modulus, shear modulus, and Poisson's ratio of the base material, respectively, and D_0 represents the relative density and is determined by

$$D_0 = \frac{\rho(\mathscr{Z})}{\rho_s}, \tag{8}$$

in which ρ_s is the mass density of the base material, and $\rho(\mathscr{Z})$ is the mass density functional grading of TPMS and depends on the porosity distribution model. Regarding the mass density functional grading of TPMS structures, the present research considers two porosity distributions along the thickness direction. Two porosity distribution patterns may be explicitly specified using the following formulae [15]:

$$\text{Pattern PA}: \; \rho(\mathscr{Z}) = \rho_{min} + (\rho_{max} - \rho_{min})\left(\frac{1}{2} + \frac{\mathscr{Z}}{h}\right)^{n_A}, \tag{9a}$$

$$\text{Pattern PB}: \; \rho(\mathscr{Z}) = \rho_{min} + (\rho_{max} - \rho_{min})\left(1 - \cos\left(\frac{\pi\mathscr{Z}}{h}\right)\right)^{n_B}. \tag{9b}$$

in where n_i denotes the pattern power index, which describes the distribution of porosity along the thickness of the panel, and ρ_{min} and ρ_{max} stand for the minimum and maximum of the relative density ρ. The power indices for these porosity patterns in this investigation may be described as follows [35]:

$$n_A = \frac{\rho_{max} - \frac{M}{\rho_s h}}{\frac{M}{\rho_s h} - \rho_{min}}, \tag{10a}$$

$$\frac{M}{\rho_b h} = \int_0^1 \frac{2\rho_{max}(1 - \rho_0 + \rho_0(1-u)^{n_B})}{\pi\sqrt{1-u^2}} \mathrm{d}u, \tag{10b}$$

in which $\rho_0 = 1 - \frac{\rho_{min}}{\rho_{max}}$ and $u = \cos\left(\frac{\pi\mathscr{Z}}{h}\right)$. Additionally, the parameter M denotes the mass per surface determined as follows

$$M = \int_{-h/2}^{h/2} \rho(\mathscr{Z})\mathrm{d}\mathscr{Z}. \tag{11}$$

The FG-TPMS plate numerical results are shown in this section. The basis material used in all of the following is Aluminum (Al), which has the following characteristics: density $\rho_s = 2702$ $[Kg/m^3]$, Young's modulus $E_s = 70$ $[GPa]$, and Poisson's ratio $\nu_s = 0.3$. Since TPMSs are made of a single solid material, it is well known that their thermal expansion coefficient is equal to the material's [36]. Based on Eq. (10), the values of the relevant parameters for these circumstances are detailed in Table 1.

3. Mathematical formulations

3.1. Displacement field of a sinusoidal shear deformation theory (SSDT)

Four independent variables are used in the research to develop the SSDT's novel sinusoidal shear deformation theory: $u(\mathscr{X}, \mathscr{Y}, \mathscr{Z}, t)$, $v(\mathscr{X}, \mathscr{Y}, \mathscr{Z}, t)$, $w(\mathscr{X}, \mathscr{Y}, \mathscr{Z}, t)$ represent the shell's displacement in the $\mathscr{X}, \mathscr{Y}, \mathscr{Z}$ directions. The displacement field of the shell may be expressed mathematically as follows:

$$u(\mathscr{X},\mathscr{Y},\mathscr{Z},t)=u_0(\mathscr{X},\mathscr{Y},t)-\mathscr{Z}\frac{\partial w_0}{\partial \mathscr{X}}+\mathscr{T}(\mathscr{Z})\left(\frac{\partial \mathfrak{Y}}{\partial \mathscr{X}}+\frac{\partial w_0}{\partial \mathscr{X}}\right), \tag{12a}$$

$$v(\mathscr{X},\mathscr{Y},\mathscr{Z},t)=v_0(\mathscr{X},\mathscr{Y},t)-\mathscr{Z}\frac{\partial w_0}{\partial \mathscr{Y}}+\mathscr{T}(\mathscr{Z})\left(\frac{\partial \mathfrak{Y}}{\partial \mathscr{Y}}+\frac{\partial w_0}{\partial \mathscr{Y}}\right), \tag{12b}$$

$$w(\mathscr{X},\mathscr{Y},\mathscr{Z},t)=w_0(\mathscr{X},\mathscr{Y},t). \tag{21c}$$

where $u_0(\mathscr{X},\mathscr{Y},t), v_0(\mathscr{X},\mathscr{Y},t), w_0(\mathscr{X},\mathscr{Y},t)$ represent the displacement in middle surface, and $\mathfrak{Y}(\mathscr{X},\mathscr{Y},t)$ represents the normal transverse rotations at $\mathscr{Z}=0$ $\left(\frac{\partial u}{\partial \mathscr{Z}}|_{\mathscr{Z}=0}=\frac{\partial \mathfrak{Y}}{\partial \mathscr{X}},\frac{\partial v}{\partial \mathscr{Z}}|_{\mathscr{Z}=0}=\frac{\partial \mathfrak{Y}}{\partial \mathscr{Y}}\right)$. The displacement field is chosen to satisfy the stress-free boundary conditions on the bottom and top surfaces of the shell $\left(\sigma_{\mathscr{X}\mathscr{Z}}|_{\mathscr{Z}=\pm h/2}=\sigma_{\mathscr{X}\mathscr{Z}}|_{\mathscr{Z}=\pm h/2}=0\right)$. In this study, $\mathscr{T}(\mathscr{Z})=-\frac{h}{\pi}\cos\left(\frac{\pi\mathscr{Z}}{h}+\frac{\pi}{2}\right)$ is nonlinear shear function that can be obtained by two conditions for displacement field equaled to $\mathscr{T}(\mathscr{Z})|_{\mathscr{Z}=0}=0, \frac{d\mathscr{T}(\mathscr{Z})}{d\mathscr{Z}}|_{\mathscr{Z}=0}=1$ and $\frac{d\mathscr{T}(\mathscr{Z})}{d\mathscr{Z}}|_{\mathscr{Z}=\pm h/2}=0$.

3.2. Constitutive relations

Von Kármán's geometric nonlinearity of doubly curved shallow shells is taken into consideration while defining the displacement–strain relationship [37]:

$$\begin{Bmatrix}\mathscr{E}_{\mathscr{X}}\\ \mathscr{E}_{\mathscr{Y}}\\ \gamma_{\mathscr{X}\mathscr{Y}}\end{Bmatrix}=\begin{Bmatrix}\frac{\partial u}{\partial \mathscr{X}}-\frac{w}{R_{\mathscr{X}}}+\frac{1}{2}\left(\frac{\partial w}{\partial \mathscr{X}}\right)^2\\ \frac{\partial v}{\partial \mathscr{Y}}-\frac{w}{R_{\mathscr{Y}}}+\frac{1}{2}\left(\frac{\partial w}{\partial \mathscr{Y}}\right)^2\\ \frac{\partial u}{\partial \mathscr{Y}}+\frac{\partial v}{\partial \mathscr{X}}+\frac{\partial w}{\partial \mathscr{X}}\frac{\partial w}{\partial \mathscr{Y}}\end{Bmatrix},\ \begin{Bmatrix}\gamma_{\mathscr{X}\mathscr{Z}}\\ \gamma_{\mathscr{Y}\mathscr{Z}}\end{Bmatrix}=\begin{Bmatrix}\frac{\partial u}{\partial \mathscr{Z}}+\frac{\partial w}{\partial \mathscr{X}}\\ \frac{\partial v}{\partial \mathscr{Z}}+\frac{\partial w}{\partial \mathscr{Y}}\end{Bmatrix}. \tag{13}$$

Substituting Eqs. (12) in Eq. (13) yields:

$$\mathscr{E}=\mathscr{E}^0+\mathscr{Z}k^1+\mathscr{T}(\mathscr{Z})k^3, \tag{14a}$$

$$\gamma=\gamma^0+\mathfrak{g}(\mathscr{Z})k^2. \tag{14b}$$

where

$$\mathscr{E}^0=\begin{Bmatrix}\mathscr{E}^0_{\mathscr{X}}\\ \mathscr{E}^0_{\mathscr{Y}}\\ \gamma^0_{\mathscr{X}\mathscr{Y}}\end{Bmatrix}=\begin{Bmatrix}\frac{\partial u_0}{\partial \mathscr{X}}-\frac{w_0}{R_{\mathscr{X}}}+\frac{1}{2}\left(\frac{\partial w_0}{\partial \mathscr{X}}\right)^2\\ \frac{\partial v_0}{\partial \mathscr{Y}}-\frac{w_0}{R_{\mathscr{Y}}}+\frac{1}{2}\left(\frac{\partial w_0}{\partial \mathscr{Y}}\right)^2\\ \frac{\partial u_0}{\partial \mathscr{Y}}+\frac{\partial v_0}{\partial \mathscr{X}}+\frac{\partial w_0}{\partial \mathscr{X}}\frac{\partial w_0}{\partial \mathscr{Y}}\end{Bmatrix},\ \gamma^0=\begin{Bmatrix}\gamma^0_{\mathscr{X}\mathscr{Z}}\\ \gamma^0_{\mathscr{Y}\mathscr{Z}}\end{Bmatrix}$$

$$=\begin{Bmatrix}\frac{\partial \mathfrak{Y}}{\partial \mathscr{X}}+\frac{\partial w_0}{\partial \mathscr{X}}\\ \frac{\partial \mathfrak{Y}}{\partial \mathscr{Y}}+\frac{\partial w_0}{\partial \mathscr{Y}}\end{Bmatrix}, \tag{15a}$$

$$k^1=\begin{Bmatrix}k^1_{\mathscr{X}}\\ k^1_{\mathscr{Y}}\\ k^1_{\mathscr{X}\mathscr{Y}}\end{Bmatrix}=\begin{Bmatrix}-\frac{\partial^2 w_0}{\partial \mathscr{X}^2}\\ -\frac{\partial^2 w_0}{\partial \mathscr{Y}^2}\\ -2\frac{\partial^2 w_0}{\partial \mathscr{X}\partial \mathscr{Y}}\end{Bmatrix},\ k^2=\begin{Bmatrix}k^2_{\mathscr{X}\mathscr{Z}}\\ k^2_{\mathscr{Y}\mathscr{Z}}\end{Bmatrix}$$

$$=\begin{Bmatrix}\frac{\partial \mathfrak{Y}}{\partial \mathscr{X}}+\frac{\partial w_0}{\partial \mathscr{X}}\\ \frac{\partial \mathfrak{Y}}{\partial \mathscr{Y}}+\frac{\partial w_0}{\partial \mathscr{Y}}\end{Bmatrix},\ \mathfrak{g}(\mathscr{Z})=\frac{d\mathscr{T}(\mathscr{Z})}{d\mathscr{Z}}-1, \tag{15b}$$

$$k^3=\begin{Bmatrix}k^3_{\mathscr{X}}\\ k^3_{\mathscr{Y}}\\ k^3_{\mathscr{X}\mathscr{Y}}\end{Bmatrix}=\begin{Bmatrix}\frac{\partial^2 \mathfrak{Y}}{\partial \mathscr{X}^2}+\frac{\partial^2 w_0}{\partial \mathscr{X}^2}\\ \frac{\partial^2 \mathfrak{Y}}{\partial \mathscr{Y}^2}+\frac{\partial^2 w_0}{\partial \mathscr{Y}^2}\\ 2\frac{\partial^2 \mathfrak{Y}}{\partial \mathscr{X}\partial \mathscr{Y}}+2\frac{\partial^2 w_0}{\partial \mathscr{X}\partial \mathscr{Y}}\end{Bmatrix}. \tag{15c}$$

The constitutive relations of the shell are given by:

$$\begin{Bmatrix}\sigma_{\mathscr{X}}\\ \sigma_{\mathscr{Y}}\\ \sigma_{\mathscr{X}\mathscr{Y}}\\ \sigma_{\mathscr{Y}\mathscr{Z}}\\ \sigma_{\mathscr{X}\mathscr{Z}}\end{Bmatrix}=\begin{Bmatrix}\mathfrak{M}_{11} & \mathfrak{M}_{12} & 0 & 0 & 0\\ \mathfrak{M}_{12} & \mathfrak{M}_{22} & 0 & 0 & 0\\ 0 & 0 & \mathfrak{M}_{66} & 0 & 0\\ 0 & 0 & 0 & \mathfrak{M}_{44} & 0\\ 0 & 0 & 0 & 0 & \mathfrak{M}_{55}\end{Bmatrix}\begin{Bmatrix}\mathscr{E}_{\mathscr{X}}\\ \mathscr{E}_{\mathscr{Y}}\\ \gamma_{\mathscr{X}\mathscr{Y}}\\ \gamma_{\mathscr{Y}\mathscr{Z}}\\ \gamma_{\mathscr{X}\mathscr{Z}}\end{Bmatrix}, \tag{16}$$

where

$$\mathfrak{M}_{11}=\frac{E(\mathscr{Z})}{1-(v(\mathscr{Z}))^2},\ \mathfrak{M}_{12}=\frac{v(\mathscr{Z})E(\mathscr{Z})}{1-(v(\mathscr{Z}))^2},\ \mathfrak{M}_{22}=\frac{E(\mathscr{Z})}{1-(v(\mathscr{Z}))^2}, \tag{17a}$$

$$\mathfrak{M}_{44}=\mathfrak{M}_{55}=\mathfrak{M}_{66}=G(\mathscr{Z}). \tag{17b}$$

3.3. Equations of motion

Hamilton's principle may be used to develop the equations of motion for the new sinusoidal deformation shear theory. The following is the definition of the virtual strain energy:

$$\delta U=\int_A\int_{-\frac{h}{2}}^{\frac{h}{2}}\left(\sigma_{\mathscr{X}}\delta\mathscr{E}_{\mathscr{X}}+\sigma_{\mathscr{Y}}\delta\mathscr{E}_{\mathscr{Y}}+\sigma_{\mathscr{X}\mathscr{Y}}\delta\gamma_{\mathscr{X}\mathscr{Y}}+\sigma_{\mathscr{X}\mathscr{Z}}\delta\gamma_{\mathscr{X}\mathscr{Z}}+\sigma_{\mathscr{Y}\mathscr{Z}}\delta\gamma_{\mathscr{Y}\mathscr{Z}}\right) d\mathscr{Z}dA. \tag{18}$$

Substituting Eq. (13) in Eq. (18) yields:

$$\delta U=\int_A\int_{-\frac{h}{2}}^{\frac{h}{2}}\begin{Bmatrix}\sigma_{\mathscr{X}}\left(\delta\mathscr{E}^0_{\mathscr{X}}+Z\delta k^1_{\mathscr{X}}+T(Z)\delta k^3_{\mathscr{X}}\right)+\sigma_{\mathscr{Y}}\left(\delta\mathscr{E}^0_{\mathscr{Y}}+Z\delta k^1_{\mathscr{Y}}+T(Z)\delta k^3_{\mathscr{Y}}\right)\\ +\sigma_{\mathscr{X}\mathscr{Y}}\left(\delta\gamma^0_{\mathscr{X}\mathscr{Y}}+Z\delta k^1_{\mathscr{X}\mathscr{Y}}+T(Z)\delta k^3_{\mathscr{X}\mathscr{Y}}\right)+\sigma_{\mathscr{X}\mathscr{Z}}\left(\delta\gamma^0_{\mathscr{X}\mathscr{Z}}+g(Z)\delta k^2_{\mathscr{X}\mathscr{Z}}\right)\\ +\sigma_{\mathscr{Y}\mathscr{Z}}\left(\delta\gamma^0_{\mathscr{Y}\mathscr{Z}}+g(Z)\delta k^2_{\mathscr{Y}\mathscr{Z}}\right)\end{Bmatrix}$$

$$=\int_A\begin{Bmatrix}\left(\mathbb{n}_{\mathscr{X}}\delta E^0_{\mathscr{X}}+\mathbb{m}_{\mathscr{X}}\delta k^1_{\mathscr{X}}+\mathbb{p}_{\mathscr{X}}\delta k^3_{\mathscr{X}}\right)+\left(\mathbb{n}_{\mathscr{Y}}\delta E^0_{\mathscr{Y}}+\mathbb{m}_{\mathscr{Y}}\delta k^1_{\mathscr{Y}}+\mathbb{p}_{\mathscr{Y}}\delta k^3_{\mathscr{Y}}\right)\\ +\left(\mathbb{n}_{\mathscr{X}\mathscr{Y}}\delta\gamma^0_{\mathscr{X}\mathscr{Y}}+\mathbb{m}_{\mathscr{X}\mathscr{Y}}\delta k^1_{\mathscr{X}\mathscr{Y}}+\mathbb{p}_{\mathscr{X}\mathscr{Y}}\delta k^3_{\mathscr{X}\mathscr{Y}}\right)\\ +\left(\mathbb{q}_{\mathscr{X}\mathscr{Z}}\delta\gamma^0_{\mathscr{X}\mathscr{Z}}+\mathbb{k}_{\mathscr{X}\mathscr{Z}}\delta k^2_{\mathscr{X}\mathscr{Z}}\right)+\left(\mathbb{q}_{\mathscr{Y}\mathscr{Z}}\delta\gamma^0_{\mathscr{Y}\mathscr{Z}}+\mathbb{k}_{\mathscr{Y}\mathscr{Z}}\delta k^2_{\mathscr{Y}\mathscr{Z}}\right)\end{Bmatrix}dA. \tag{19}$$

where

$$(\mathbb{n}_i, \mathbb{m}_i, \mathbb{p}_i) = \int_{-\frac{h}{2}}^{\frac{h}{2}} \sigma_i(1, \mathcal{Z}, \mathcal{T}(\mathcal{Z}))\mathrm{d}\mathcal{Z}, \ \{i = \mathcal{X}, \mathcal{Y}, \mathcal{X}\mathcal{Y}\} \tag{20a}$$

$$(\mathbb{q}_i, \mathbb{k}_i) = \int_{-\frac{h}{2}}^{\frac{h}{2}} \sigma_i(1, \mathbb{g}(\mathcal{Z}))\mathrm{d}\mathcal{Z}, \ \{j = \mathcal{X}\mathcal{Z}, \mathcal{Y}\mathcal{Z}\} \tag{20b}$$

Substituting Eqs. (15a), (15b), (15c) and (16) in Eqs. (20a), and (20b) leads to:

$$\begin{Bmatrix} n \\ m \\ p \end{Bmatrix} = \begin{bmatrix} [\mathfrak{A}] & [\mathfrak{B}] & [\mathfrak{D}] \\ [\mathfrak{B}] & [\mathfrak{C}] & [\mathfrak{E}] \\ [\mathfrak{D}] & [\mathfrak{E}] & [\mathfrak{G}] \end{bmatrix} \begin{Bmatrix} \mathcal{E}^0 \\ k^1 \\ k^3 \end{Bmatrix}, \tag{21a}$$

$$\begin{Bmatrix} q \\ k \end{Bmatrix} = \begin{bmatrix} [\mathfrak{A}_s] & [\mathfrak{C}_s] \\ [\mathfrak{C}_s] & [\mathfrak{E}_s] \end{bmatrix} \begin{Bmatrix} \gamma^0 \\ k^2 \end{Bmatrix}, \tag{21b}$$

where

$$[\mathfrak{A}] = \begin{bmatrix} \mathfrak{A}_{11} & \mathfrak{A}_{12} & 0 \\ \mathfrak{A}_{12} & \mathfrak{A}_{22} & 0 \\ 0 & 0 & \mathfrak{A}_{66} \end{bmatrix}, \ [\mathfrak{B}] = \begin{bmatrix} \mathfrak{B}_{11} & \mathfrak{B}_{12} & 0 \\ \mathfrak{B}_{12} & \mathfrak{B}_{22} & 0 \\ 0 & 0 & \mathfrak{B}_{66} \end{bmatrix}, \ [\mathfrak{C}] = \begin{bmatrix} \mathfrak{C}_{11} & \mathfrak{C}_{12} & 0 \\ \mathfrak{C}_{12} & \mathfrak{C}_{22} & 0 \\ 0 & 0 & \mathfrak{C}_{66} \end{bmatrix}, \tag{22a}$$

$$[\mathfrak{D}] = \begin{bmatrix} \mathfrak{D}_{11} & \mathfrak{D}_{12} & 0 \\ \mathfrak{D}_{12} & \mathfrak{D}_{22} & 0 \\ 0 & 0 & \mathfrak{D}_{66} \end{bmatrix}, \ [\mathfrak{E}] = \begin{bmatrix} \mathfrak{E}_{11} & \mathfrak{E}_{12} & 0 \\ \mathfrak{E}_{12} & \mathfrak{E}_{22} & 0 \\ 0 & 0 & \mathfrak{E}_{66} \end{bmatrix}, \ [\mathfrak{G}] = \begin{bmatrix} \mathfrak{G}_{11} & \mathfrak{G}_{12} & 0 \\ \mathfrak{G}_{12} & \mathfrak{G}_{22} & 0 \\ 0 & 0 & \mathfrak{G}_{66} \end{bmatrix}, \tag{22b}$$

$$[\mathfrak{A}_s] = \begin{bmatrix} \mathfrak{A}_{44} & 0 \\ 0 & \mathfrak{A}_{55} \end{bmatrix}, \ [\mathfrak{C}_s] = \begin{bmatrix} \mathfrak{C}_{44} & 0 \\ 0 & \mathfrak{C}_{55} \end{bmatrix}, \ [\mathfrak{E}_s] = \begin{bmatrix} \mathfrak{E}_{44} & 0 \\ 0 & \mathfrak{E}_{55} \end{bmatrix}, \tag{22c}$$

$$(\mathfrak{A}_{ij}, \mathfrak{B}_{ij}, \mathfrak{C}_{ij}, \mathfrak{D}_{ij}, \mathfrak{E}_{ij}, \mathfrak{G}_{ij}) = \int_{-\frac{h}{2}}^{\frac{h}{2}} \mathbb{q}_{ij}\left(1, \mathcal{Z}, \mathcal{Z}^2, \mathcal{T}(\mathcal{Z}), \mathcal{Z}\mathcal{T}(\mathcal{Z}), \mathcal{T}^2(\mathcal{Z})\right) \mathrm{d}\mathcal{Z}, (i, j = 1\text{to}6), \tag{22d}$$

$$\left(\mathfrak{A}_{sij}, \mathfrak{C}_{sij}, \mathfrak{E}_{sij}\right) = \int_{-\frac{h}{2}}^{\frac{h}{2}} \mathbb{q}_{ij}\left(1, \mathbb{g}(\mathcal{Z}), \mathbb{g}^2(\mathcal{Z})\right)\mathrm{d}\mathcal{Z}, (ij = 44, 55). \tag{22e}$$

The virtual work done by applied forces is determined by:

$$\delta V = -\int_A (q(t)\delta \mathscr{w}_0)\mathrm{d}A, \tag{23}$$

where $q(t)$ represents the external force. Also, we have $q(t) = q_0\sin(\Omega t)$ or $q(t) = q_0\sin(\Omega t)$, in which q_0, and Ω, shows the intensity load, and excitation frequency of the system.

The virtual kinetic energy is given by:

$$\begin{aligned}
\delta K =& \int_A \int_{-\frac{h}{2}}^{\frac{h}{2}} \rho(\mathcal{Z})(\dot{\mathscr{u}}\delta\dot{\mathscr{u}} + \dot{\mathscr{v}}\delta\dot{\mathscr{v}} + \dot{\mathscr{w}}\delta\dot{\mathscr{w}})\mathrm{d}\mathcal{Z}\,\mathrm{d}\mathfrak{A} = \\
=& \int_A \Bigg\{ \mathcal{L}_0(\dot{\mathscr{u}}_0\delta\dot{\mathscr{u}}_0 + \dot{\mathscr{v}}_0\delta\dot{\mathscr{v}}_0 + \dot{\mathscr{w}}_0\delta\dot{\mathscr{w}}_0) - \mathcal{L}_1\left(\dot{\mathscr{u}}_0\frac{\partial\delta\dot{\mathscr{w}}_0}{\partial\mathcal{X}} + \frac{\partial\dot{\mathscr{w}}_0}{\partial\mathcal{X}}\delta\dot{\mathscr{u}}_0 + \dot{\mathscr{v}}_0\frac{\partial\delta\dot{\mathscr{w}}_0}{\partial\mathcal{Y}} + \frac{\partial\dot{\mathscr{w}}_0}{\partial\mathcal{Y}}\delta\dot{\mathscr{v}}_0\right) + \mathcal{L}_2\left(\frac{\partial\dot{\mathscr{w}}_0}{\partial\mathcal{X}}\frac{\partial\delta\dot{\mathscr{w}}_0}{\partial\mathcal{X}} + \frac{\partial\dot{\mathscr{w}}_0}{\partial\mathcal{Y}}\frac{\partial\delta\dot{\mathscr{w}}_0}{\partial\mathcal{Y}}\right) \\
&+J_1\left(\begin{array}{l} \dot{\mathscr{u}}_0\left(\frac{\partial\delta\dot{\mathfrak{Y}}}{\partial\mathcal{X}} + \frac{\partial\delta\dot{\mathscr{w}}_0}{\partial\mathcal{X}}\right) + \delta\dot{\mathscr{u}}_0\left(\frac{\partial\dot{\mathfrak{Y}}}{\partial\mathcal{X}} + \frac{\partial\dot{\mathscr{w}}_0}{\partial\mathcal{X}}\right) \\ +\dot{\mathscr{v}}_0\left(\frac{\partial\delta\dot{\mathfrak{Y}}}{\partial\mathcal{Y}} + \frac{\partial\delta\dot{\mathscr{w}}_0}{\partial\mathcal{Y}}\right) + \delta\dot{\mathscr{v}}_0\left(\frac{\partial\dot{\mathfrak{Y}}}{\partial\mathcal{Y}} + \frac{\partial\dot{\mathscr{w}}_0}{\partial\mathcal{Y}}\right) \end{array}\right) \\
&-J_2\left(\begin{array}{l} \frac{\partial\delta\dot{\mathscr{w}}_0}{\partial\mathcal{X}}\left(\frac{\partial\dot{\mathfrak{Y}}}{\partial\mathcal{X}} + \frac{\partial\dot{\mathscr{w}}_0}{\partial\mathcal{X}}\right) + \frac{\partial\dot{\mathscr{w}}_0}{\partial\mathcal{X}}\left(\frac{\partial\delta\dot{\mathfrak{Y}}}{\partial\mathcal{X}} + \frac{\partial\delta\dot{\mathscr{w}}_0}{\partial\mathcal{X}}\right) \\ +\frac{\partial\dot{\mathscr{w}}_0}{\partial\mathcal{Y}}\left(\frac{\partial\delta\dot{\mathfrak{Y}}}{\partial\mathcal{Y}} + \frac{\partial\delta\dot{\mathscr{w}}_0}{\partial\mathcal{Y}}\right) + \frac{\partial\delta\dot{\mathscr{w}}_0}{\partial\mathcal{Y}}\left(\frac{\partial\dot{\mathfrak{Y}}}{\partial\mathcal{Y}} + \frac{\partial\dot{\mathscr{w}}_0}{\partial\mathcal{Y}}\right) \end{array}\right) \\
&+J_3\left(\left(\frac{\partial\delta\dot{\mathfrak{Y}}}{\partial\mathcal{X}} + \frac{\partial\delta\dot{\mathscr{w}}_0}{\partial\mathcal{X}}\right)\left(\frac{\partial\dot{\mathfrak{Y}}}{\partial\mathcal{X}} + \frac{\partial\dot{\mathscr{w}}_0}{\partial\mathcal{X}}\right) + \left(\frac{\partial\dot{\mathfrak{Y}}}{\partial\mathcal{Y}} + \frac{\partial\dot{\mathscr{w}}_0}{\partial\mathcal{Y}}\right)\left(\frac{\partial\delta\dot{\mathfrak{Y}}}{\partial\mathcal{Y}} + \frac{\partial\delta\dot{\mathscr{w}}_0}{\partial\mathcal{Y}}\right)\right)\Bigg\}\mathrm{d}A,
\end{aligned} \tag{24}$$

where mass inertias are defined by:

$$\{\mathcal{L}_0, \mathcal{L}_1, \mathcal{L}_2, J_1, J_2, J_3\} = \int_{-\frac{h}{2}}^{\frac{h}{2}} \rho(\mathcal{Z})\{1, \mathcal{Z}, \mathcal{Z}^2, \mathcal{T}(\mathcal{Z}), \mathcal{Z}\mathcal{T}(\mathcal{Z}), \mathcal{T}^2(\mathcal{Z})\} \mathrm{d}\mathcal{Z}. \tag{25}$$

Hamilton's principle can be stated in analytical form as:

$$\int_0^T (\delta U + \delta V - \delta K)\mathrm{d}t = 0, \tag{26}$$

Replacing Eqs. (19), (23), and (24) in Eq. (26) and integrating by parts obtain the following Euler–Lagrange equations:

$$\delta\mathscr{u}_0 : \mathbb{n}_{\mathcal{X},\mathcal{X}} + \mathbb{n}_{\mathcal{X}\mathcal{Y},\mathcal{Y}} = \mathcal{L}_0\ddot{\mathscr{u}}_0 + (J_1 - \mathcal{L}_1)\frac{\partial\ddot{\mathscr{w}}_0}{\partial\mathcal{X}} + J_1\frac{\partial\ddot{\mathfrak{Y}}}{\partial\mathcal{X}}, \tag{27a}$$

$$\delta v_0 : \mathbb{n}_{\mathscr{Y},\mathscr{Y}} + \mathbb{n}_{\mathscr{X}\mathscr{Y},\mathscr{X}} = \mathscr{L}_0 \ddot{v}_0 + (J_1 - \mathscr{L}_1)\frac{\partial \ddot{w}_0}{\partial \mathscr{Y}} + J_1 \frac{\partial \ddot{\mathfrak{Y}}}{\partial \mathscr{Y}}, \tag{27b}$$

$$\begin{aligned}\delta w_0 :\ & \left(\frac{\mathbb{n}_{\mathscr{X}}}{R_{\mathscr{X}}} + \frac{\mathbb{n}_{\mathscr{Y}}}{R_{\mathscr{Y}}}\right) + \left(\mathbb{m}_{\mathscr{X},\mathscr{X}\mathscr{X}} + \mathbb{m}_{\mathscr{Y},\mathscr{Y}\mathscr{Y}} + 2\mathbb{m}_{\mathscr{X}\mathscr{Y},\mathscr{X}\mathscr{Y}}\right) - \left(\mathbb{p}_{\mathscr{X},\mathscr{X}\mathscr{X}} + \mathbb{p}_{\mathscr{Y},\mathscr{Y}\mathscr{Y}} + 2\mathbb{p}_{\mathscr{X}\mathscr{Y},\mathscr{X}\mathscr{Y}}\right) + \left(\mathbb{q}_{\mathscr{X}\mathscr{Z},\mathscr{X}} + \mathbb{q}_{\mathscr{Y}\mathscr{Z},\mathscr{Y}} + \mathbb{k}_{\mathscr{X}\mathscr{Z},\mathscr{X}} + \mathbb{k}_{\mathscr{Y}\mathscr{Z},\mathscr{Y}}\right) \\ & + \frac{\partial}{\partial \mathscr{X}}\left(\mathbb{n}_{\mathscr{X}}\frac{\partial w_0}{\partial \mathscr{X}} + \mathbb{n}_{\mathscr{X}\mathscr{Y}}\frac{\partial w_0}{\partial \mathscr{Y}}\right) + \frac{\partial}{\partial \mathscr{Y}}\left(\mathbb{n}_{\mathscr{Y}}\frac{\partial w_0}{\partial \mathscr{Y}} + \mathbb{n}_{\mathscr{X}\mathscr{Y}}\frac{\partial w_0}{\partial \mathscr{X}}\right) + q = \mathscr{L}_0 \ddot{w}_0 + \mathscr{L}_1\left(\frac{\partial \ddot{u}_0}{\partial \mathscr{X}} + \frac{\partial \ddot{v}_0}{\partial \mathscr{Y}}\right) - \mathscr{L}_2\left(\frac{\partial^2 \ddot{w}_0}{\partial \mathscr{X}^2} + \frac{\partial^2 \ddot{w}_0}{\partial \mathscr{Y}^2}\right) \\ & - J_1\left(\frac{\partial \ddot{u}_0}{\partial \mathscr{X}} + \frac{\partial \ddot{v}_0}{\partial \mathscr{Y}}\right) + J_2\left(2\frac{\partial^2 \ddot{w}_0}{\partial \mathscr{X}^2} + 2\frac{\partial^2 \ddot{w}_0}{\partial \mathscr{Y}^2} + \frac{\partial^2 \ddot{\mathfrak{Y}}}{\partial \mathscr{Y}^2} + \frac{\partial^2 \ddot{\mathfrak{Y}}}{\partial \mathscr{X}^2}\right) - J_3\left(\frac{\partial^2 \ddot{w}_0}{\partial \mathscr{X}^2} + \frac{\partial^2 \ddot{w}_0}{\partial \mathscr{Y}^2} + \frac{\partial^2 \ddot{\mathfrak{Y}}}{\partial \mathscr{X}^2} + \frac{\partial^2 \ddot{\mathfrak{Y}}}{\partial \mathscr{Y}^2}\right)\end{aligned} \tag{27c}$$

$$\begin{aligned}\delta \mathfrak{Y} :\ & \left(\mathbb{p}_{\mathscr{X},\mathscr{X}\mathscr{X}} + 2\mathbb{p}_{\mathscr{X}\mathscr{Y},\mathscr{X}\mathscr{Y}} + \mathbb{p}_{\mathscr{Y},\mathscr{Y}\mathscr{Y}}\right) \\ & - \left(\mathbb{q}_{\mathscr{X}\mathscr{Z},\mathscr{X}} + \mathbb{q}_{\mathscr{Y}\mathscr{Z},\mathscr{Y}} + \mathbb{k}_{\mathscr{X}\mathscr{Z},\mathscr{X}} + \mathbb{k}_{\mathscr{Y}\mathscr{Z},\mathscr{Y}}\right) \\ & = J_1\left(\frac{\partial \ddot{v}_0}{\partial \mathscr{Y}} + \frac{\partial \ddot{u}_0}{\partial \mathscr{X}}\right) + (J_3 - J_2)\left(\frac{\partial^2 \ddot{w}_0}{\partial \mathscr{X}^2} + \frac{\partial^2 \ddot{w}_0}{\partial \mathscr{Y}^2}\right) + J_3\left(\frac{\partial^2 \ddot{\mathfrak{Y}}}{\partial \mathscr{X}^2} + \frac{\partial^2 \ddot{\mathfrak{Y}}}{\partial \mathscr{Y}^2}\right).\end{aligned} \tag{27d}$$

Applying a stress function $\mathscr{T}(\mathscr{X}, \mathscr{Y}, t)$ to the force resultants:

$$\mathbb{n}_{\mathscr{X}} = \frac{\partial^2 \mathscr{T}}{\partial \mathscr{Y}^2},\ \mathbb{n}_{\mathscr{Y}} = \frac{\partial^2 \mathscr{T}}{\partial \mathscr{X}^2},\ \mathbb{n}_{\mathscr{X}\mathscr{Y}} = -\frac{\partial^2 \mathscr{T}}{\partial \mathscr{X}\partial \mathscr{Y}}. \tag{28}$$

The in-plane strains should be compatible with the following condition [37]:

$$\frac{\partial^2 \mathscr{E}^0_{\mathscr{X}}}{\partial \mathscr{Y}^2} + \frac{\partial^2 \mathscr{E}^0_{\mathscr{Y}}}{\partial \mathscr{X}^2} - \frac{\partial^2 \gamma^0_{\mathscr{X}\mathscr{Y}}}{\partial \mathscr{X}\partial \mathscr{Y}} = \left(\frac{\partial^2 w_0}{\partial \mathscr{X}\partial \mathscr{Y}}\right)^2 - \frac{\partial^2 w_0}{\partial \mathscr{X}^2}\frac{\partial^2 w_0}{\partial \mathscr{Y}^2} - \frac{1}{R_{\mathscr{X}}}\frac{\partial^2 w_0}{\partial \mathscr{Y}^2} - \frac{1}{R_{\mathscr{Y}}}\frac{\partial^2 w_0}{\partial \mathscr{X}^2}. \tag{29}$$

By substituting Airy's stress function in Eq. (28) in Eq. (21a) to obtain in-plane strains as a function of $\mathscr{T}(\mathscr{X}, \mathscr{Y}, t)$ variable, the results are satisfied by the geometrical compatibility Eq. (29), as it is rewritten:

$$\begin{aligned}& \mathfrak{H}_{11}\frac{\partial^4 \mathscr{T}}{\partial \mathscr{X}^4} + \mathfrak{H}_{12}\frac{\partial^4 \mathscr{T}}{\partial \mathscr{Y}^4} + \mathfrak{H}_{13}\frac{\partial^4 \mathscr{T}}{\partial \mathscr{X}^2\partial \mathscr{Y}^2} + \mathfrak{H}_{14}\frac{\partial^4 w_0}{\partial \mathscr{X}^4} + \mathfrak{H}_{15}\frac{\partial^4 w_0}{\partial \mathscr{Y}^4} \\ & + \mathfrak{H}_{16}\frac{\partial^4 w_0}{\partial \mathscr{X}^2\partial \mathscr{Y}^2} + \mathfrak{H}_{17}\frac{\partial^4 \mathfrak{Y}}{\partial \mathscr{X}^4} + \mathfrak{H}_{18}\frac{\partial^4 \mathfrak{Y}}{\partial \mathscr{Y}^4} + \mathfrak{H}_{19}\frac{\partial^4 \mathfrak{Y}}{\partial \mathscr{X}^2\partial \mathscr{Y}^2} \\ & = \left(\frac{\partial^2 w_0}{\partial \mathscr{X}\partial \mathscr{Y}}\right)^2 - \frac{\partial^2 w_0}{\partial \mathscr{X}^2}\frac{\partial^2 w_0}{\partial \mathscr{Y}^2} - \frac{1}{R_{\mathscr{X}}}\frac{\partial^2 w_0}{\partial \mathscr{Y}^2} - \frac{1}{R_{\mathscr{Y}}}\frac{\partial^2 w_0}{\partial \mathscr{X}^2},\end{aligned} \tag{30}$$

where

$$\mathfrak{H}_{11} = \frac{\mathfrak{A}_{11}}{\mathfrak{A}_{11}\mathfrak{A}_{22} - \mathfrak{A}_{12}^2}, \mathfrak{H}_{12} = \frac{\mathfrak{A}_{22}}{\mathfrak{A}_{11}\mathfrak{A}_{22} - \mathfrak{A}_{12}^2}, \mathfrak{H}_{13} = \frac{1}{\mathfrak{A}_{66}} - \frac{2\mathfrak{A}_{12}}{\mathfrak{A}_{11}\mathfrak{A}_{22} - \mathfrak{A}_{12}^2}, \tag{31a}$$

$$\mathfrak{H}_{14} = \frac{\mathfrak{A}_{11}\mathfrak{B}_{12} - \mathfrak{A}_{12}\mathfrak{B}_{11} + \mathfrak{A}_{12}\mathfrak{D}_{11} - \mathfrak{A}_{11}\mathfrak{D}_{12}}{\mathfrak{A}_{11}\mathfrak{A}_{22} - \mathfrak{A}_{12}^2}, \mathfrak{H}_{15} = \frac{\mathfrak{A}_{22}\mathfrak{B}_{12} - \mathfrak{A}_{12}\mathfrak{B}_{22} + \mathfrak{A}_{12}\mathfrak{D}_{22} - \mathfrak{A}_{22}\mathfrak{D}_{12}}{\mathfrak{A}_{11}\mathfrak{A}_{22} - \mathfrak{A}_{12}^2}, \tag{31b}$$

$$\mathfrak{H}_{16} = \frac{\mathfrak{A}_{22}\mathfrak{B}_{11} - 2\mathfrak{A}_{12}\mathfrak{B}_{12} + 2\mathfrak{A}_{12}\mathfrak{D}_{12} - \mathfrak{A}_{11}\mathfrak{D}_{22} + \mathfrak{A}_{11}\mathfrak{B}_{22} - \mathfrak{A}_{22}\mathfrak{D}_{11}}{\mathfrak{A}_{11}\mathfrak{A}_{22} - \mathfrak{A}_{12}^2} - \frac{2\mathfrak{B}_{66}}{\mathfrak{A}_{66}} + \frac{2\mathfrak{D}_{66}}{\mathfrak{A}_{66}}, \tag{31c}$$

$$\mathfrak{H}_{17} = \frac{\mathfrak{A}_{12}\mathfrak{D}_{11} - \mathfrak{A}_{11}\mathfrak{D}_{12}}{\mathfrak{A}_{11}\mathfrak{A}_{22} - \mathfrak{A}_{12}^2}, \mathfrak{H}_{18} = \frac{\mathfrak{A}_{12}\mathfrak{D}_{22} - \mathfrak{A}_{22}\mathfrak{D}_{12}}{\mathfrak{A}_{11}\mathfrak{A}_{22} - \mathfrak{A}_{12}^2},\ \mathfrak{H}_{19} = \frac{2\mathfrak{A}_{12}\mathfrak{D}_{12} - \mathfrak{A}_{11}\mathfrak{D}_{22} - \mathfrak{A}_{22}\mathfrak{D}_{11}}{\mathfrak{A}_{11}\mathfrak{A}_{22} - \mathfrak{A}_{12}^2} + \frac{2\mathfrak{D}_{66}}{\mathfrak{A}_{66}}, \tag{31d}$$

Substitution of Eq. (28) in Eqs. (27a), (27b) leads to:

$$\frac{\partial^2 u_0}{\partial t^2} = \frac{(\mathscr{L}_1 - J_1)}{\mathscr{L}_0}\frac{\partial \ddot{w}_0}{\partial \mathscr{X}} - \frac{J_1}{\mathscr{L}_0}\frac{\partial \ddot{\mathfrak{Y}}}{\partial \mathscr{X}}, \tag{32a}$$

$$\frac{\partial^2 v_0}{\partial t^2} = \frac{(\mathscr{L}_1 - J_1)}{\mathscr{L}_0}\frac{\partial \ddot{w}_0}{\partial \mathscr{Y}} - \frac{J_1}{\mathscr{L}_0}\frac{\partial \ddot{\mathfrak{Y}}}{\partial \mathscr{Y}}. \tag{32b}$$

Introducing the stress function in Eqs. (28), (32a), (32b) in Eqs. (27c), (27d) gives as:

$$\begin{aligned}& \mathfrak{H}_{17}\frac{\partial^4 \mathscr{T}}{\partial \mathscr{X}^4} + \mathfrak{H}_{21}\frac{\partial^4 \mathscr{T}}{\partial \mathscr{Y}^4} + \mathfrak{H}_{22}\frac{\partial^4 \mathscr{T}}{\partial \mathscr{X}^2\partial \mathscr{Y}^2} + \mathfrak{H}_{23}\frac{\partial^4 w_0}{\partial \mathscr{X}^4} + \mathfrak{H}_{24}\frac{\partial^4 w_0}{\partial \mathscr{Y}^4} + \mathfrak{H}_{25}\frac{\partial^4 w_0}{\partial \mathscr{X}^2\partial \mathscr{Y}^2} + \mathfrak{H}_{26}\frac{\partial^4 \mathfrak{Y}}{\partial \mathscr{X}^4} + \mathfrak{H}_{27}\frac{\partial^4 \mathfrak{Y}}{\partial \mathscr{Y}^4} + \mathfrak{H}_{28}\frac{\partial^4 \mathfrak{Y}}{\partial \mathscr{X}^2\partial \mathscr{Y}^2} \\ & + \mathfrak{H}_{29}\frac{\partial^2 \mathfrak{Y}}{\partial \mathscr{X}^2} + \mathfrak{H}_{30}\frac{\partial^2 \mathfrak{Y}}{\partial \mathscr{Y}^2} + \mathfrak{H}_{29}\frac{\partial^2 w_0}{\partial \mathscr{X}^2} + \mathfrak{H}_{30}\frac{\partial^2 w_0}{\partial \mathscr{Y}^2}\left(\frac{\partial^2 w_0}{\partial \mathscr{Y}^2} + \frac{1}{R_{\mathscr{Y}}}\right)\frac{\partial^2 \mathscr{T}}{\partial \mathscr{X}^2} - 2\frac{\partial^2 \mathscr{T}}{\partial \mathscr{X}\partial \mathscr{Y}}\frac{\partial^2 w}{\partial \mathscr{X}\partial \mathscr{Y}} + \left(\frac{\partial^2 w_0}{\partial \mathscr{X}^2} + \frac{1}{R_{\mathscr{X}}}\right)\frac{\partial^2 \mathscr{T}}{\partial \mathscr{Y}^2} + q = \mathscr{L}_0 \ddot{w}_0 \\ & + \mathscr{L}_1\left(\frac{\partial \ddot{u}_0}{\partial \mathscr{X}} + \frac{\partial \ddot{v}_0}{\partial \mathscr{Y}}\right) - \mathscr{L}_2\left(\frac{\partial^2 \ddot{w}_0}{\partial \mathscr{X}^2} + \frac{\partial^2 \ddot{w}_0}{\partial \mathscr{Y}^2}\right) - J_1\left(\frac{\partial \ddot{u}_0}{\partial \mathscr{X}} + \frac{\partial \ddot{v}_0}{\partial \mathscr{Y}}\right) + J_2\left(2\frac{\partial^2 \ddot{w}_0}{\partial \mathscr{X}^2} + 2\frac{\partial^2 \ddot{w}_0}{\partial \mathscr{Y}^2} + \frac{\partial^2 \ddot{\mathfrak{Y}}}{\partial \mathscr{Y}^2} + \frac{\partial^2 \ddot{\mathfrak{Y}}}{\partial \mathscr{X}^2}\right) \\ & - J_3\left(\frac{\partial^2 \ddot{w}_0}{\partial \mathscr{X}^2} + \frac{\partial^2 \ddot{w}_0}{\partial \mathscr{Y}^2} + \frac{\partial^2 \ddot{\mathfrak{Y}}}{\partial \mathscr{X}^2} + \frac{\partial^2 \ddot{\mathfrak{Y}}}{\partial \mathscr{Y}^2}\right)\end{aligned} \tag{33a}$$

$$
\begin{aligned}
&-\mathfrak{H}_{17}\frac{\partial^4\mathscr{T}}{\partial\mathscr{X}^4}-\mathfrak{H}_{18}\frac{\partial^4\mathscr{T}}{\partial\mathscr{Y}^4}-\mathfrak{H}_{19}\frac{\partial^4\mathscr{T}}{\partial\mathscr{X}^2\partial\mathscr{Y}^2}+\mathfrak{H}_{31}\frac{\partial^4 w_0}{\partial\mathscr{X}^4}+\mathfrak{H}_{32}\frac{\partial^4 w_0}{\partial\mathscr{Y}^4}\\
&+\mathfrak{H}_{33}\frac{\partial^4 w_0}{\partial\mathscr{X}^2\partial\mathscr{Y}^2}+\mathfrak{H}_{34}\frac{\partial^4\mathfrak{Y}}{\partial\mathscr{X}^4}+\mathfrak{H}_{35}\frac{\partial^4\mathfrak{Y}}{\partial\mathscr{Y}^4}+\mathfrak{H}_{36}\frac{\partial^4\mathfrak{Y}}{\partial\mathscr{X}^2\partial\mathscr{Y}^2}+\mathfrak{H}_{37}\frac{\partial^2 w_0}{\partial\mathscr{X}^2}\\
&+\mathfrak{H}_{38}\frac{\partial^2 w_0}{\partial\mathscr{Y}^2}+\mathfrak{H}_{37}\frac{\partial^2\mathfrak{Y}}{\partial\mathscr{X}^2}+\mathfrak{H}_{38}\frac{\partial^2\mathfrak{Y}}{\partial\mathscr{Y}^2}\\
&=J_1\left(\frac{\partial\ddot{v}_0}{\partial\mathscr{Y}}+\frac{\partial\ddot{u}_0}{\partial\mathscr{X}}\right)+(J_3-J_2)\left(\frac{\partial^2\ddot{w}_0}{\partial\mathscr{X}^2}+\frac{\partial^2\ddot{w}_0}{\partial\mathscr{Y}^2}\right)+J_3\left(\frac{\partial^2\ddot{\mathfrak{Y}}}{\partial\mathscr{X}^2}+\frac{\partial^2\ddot{\mathfrak{Y}}}{\partial\mathscr{Y}^2}\right),
\end{aligned}
\tag{33b}
$$

where $\mathfrak{H}_{ij}(i=2\text{to}3, j=0\text{to}9)$ are given in Eqs. (34a)-(34p).

$$
\mathfrak{H}_{23}=\mathfrak{E}_{11}-\mathfrak{G}_{11}-\frac{\begin{pmatrix}\mathfrak{A}_{11}\mathfrak{B}_{12}\mathfrak{D}_{12}-\mathfrak{A}_{11}\mathfrak{D}_{12}^2-\mathfrak{A}_{12}\mathfrak{B}_{11}\mathfrak{D}_{12}-\mathfrak{A}_{12}\mathfrak{B}_{12}\mathfrak{D}_{11}\\+2\mathfrak{A}_{12}\mathfrak{D}_{11}\mathfrak{D}_{12}+\mathfrak{A}_{22}\mathfrak{B}_{11}\mathfrak{D}_{11}-\mathfrak{A}_{22}\mathfrak{D}_{11}^2\end{pmatrix}}{\mathfrak{A}_{11}\mathfrak{A}_{22}-\mathfrak{A}_{12}^2},
\tag{34c}
$$

$$
\mathfrak{H}_{24}=-\frac{\begin{pmatrix}\mathfrak{A}_{11}\mathfrak{A}_{22}\mathfrak{C}_{22}-2\mathfrak{A}_{11}\mathfrak{A}_{22}\mathfrak{E}_{22}+\mathfrak{A}_{11}\mathfrak{A}_{22}\mathfrak{G}_{22}-\mathfrak{A}_{11}\mathfrak{B}_{22}^2+2\mathfrak{A}_{11}\mathfrak{B}_{22}\mathfrak{D}_{22}\\-\mathfrak{A}_{11}\mathfrak{D}_{22^2}-\mathfrak{A}_{12}^2\mathfrak{C}_{22}+2\mathfrak{A}_{12}^2\mathfrak{E}_{22}-\mathfrak{A}_{12}^2\mathfrak{G}_{22}+2\mathfrak{A}_{12}\mathfrak{B}_{12}\mathfrak{B}_{22}-2\mathfrak{A}_{12}\mathfrak{B}_{12}\mathfrak{D}_{22}\\-2\mathfrak{A}_{12}\mathfrak{B}_{22}\mathfrak{D}_{12}+2\mathfrak{A}_{12}\mathfrak{D}_{12}\mathfrak{D}_{22}-\mathfrak{A}_{22}\mathfrak{B}_{12}^2+2\mathfrak{A}_{22}\mathfrak{B}_{12}\mathfrak{D}_{12}-\mathfrak{A}_{22}\mathfrak{D}_{12}^2\end{pmatrix}}{\mathfrak{A}_{11}\mathfrak{A}_{22}-\mathfrak{A}_{12}^2},
\tag{34d}
$$

$$
\begin{aligned}
\mathfrak{H}_{25}\quad&=\frac{\begin{pmatrix}+\mathfrak{A}_{11}\mathfrak{B}_{12}\mathfrak{B}_{22}-\mathfrak{A}_{11}\mathfrak{B}_{12}\mathfrak{D}_{22}-2\mathfrak{A}_{11}\mathfrak{B}_{22}\mathfrak{D}_{12}+2\mathfrak{A}_{11}\mathfrak{D}_{12}\mathfrak{D}_{22}-\mathfrak{A}_{12}\mathfrak{B}_{11}\mathfrak{B}_{22}\\+\mathfrak{A}_{12}\mathfrak{B}_{11}\mathfrak{D}_{22}-\mathfrak{A}_{12}\mathfrak{B}_{12}^2+3\mathfrak{A}_{12}\mathfrak{B}_{12}\mathfrak{D}_{12}+2\mathfrak{A}_{12}\mathfrak{B}_{22}\mathfrak{D}_{11}-2\mathfrak{A}_{12}\mathfrak{D}_{11}\mathfrak{D}_{22}\\-2\mathfrak{A}_{12}\mathfrak{D}_{12}^2+\mathfrak{A}_{22}\mathfrak{B}_{11}\mathfrak{B}_{12}-\mathfrak{A}_{22}\mathfrak{B}_{11}\mathfrak{D}_{12}-2\mathfrak{A}_{22}\mathfrak{B}_{12}\mathfrak{D}_{11}+2\mathfrak{A}_{22}\mathfrak{D}_{11}\mathfrak{D}_{12}\end{pmatrix}}{\mathfrak{A}_{11}\mathfrak{A}_{22}-\mathfrak{A}_{12}^2},\\
&\quad+4\frac{(\mathfrak{B}_{66}-\mathfrak{D}_{66})^2}{\mathfrak{A}_{66}}-4\mathfrak{C}_{66}-4\mathfrak{G}_{66}+3\mathfrak{E}_{12}+8\mathfrak{E}_{66}-2\mathfrak{G}_{12}-\mathfrak{C}_{12}
\end{aligned}
\tag{34e}
$$

$$
\mathfrak{H}_{21}=\frac{\mathfrak{A}_{22}\mathfrak{B}_{12}-\mathfrak{A}_{12}\mathfrak{B}_{22}+\mathfrak{A}_{12}\mathfrak{D}_{22}-\mathfrak{A}_{22}\mathfrak{D}_{12}}{\mathfrak{A}_{11}\mathfrak{A}_{22}-\mathfrak{A}_{12}^2},
\tag{34a}
$$

$$
\mathfrak{H}_{26}=\frac{\mathfrak{A}_{11}\mathfrak{D}_{12}^2-2\mathfrak{A}_{12}\mathfrak{D}_{11}\mathfrak{D}_{12}+\mathfrak{A}_{22}\mathfrak{D}_{11}^2}{\mathfrak{A}_{11}\mathfrak{A}_{22}-\mathfrak{A}_{12}^2}-\mathfrak{G}_{11},
\tag{34f}
$$

$$
\mathfrak{H}_{27}=\frac{\begin{pmatrix}\mathfrak{A}_{11}\mathfrak{A}_{22}\mathfrak{E}_{22}-\mathfrak{A}_{11}\mathfrak{A}_{22}\mathfrak{G}_{22}-\mathfrak{A}_{11}\mathfrak{B}_{22}\mathfrak{D}_{22}+\mathfrak{A}_{11}\mathfrak{D}_{22}^2-\mathfrak{A}_{12}^2\mathfrak{E}_{22}+\mathfrak{A}_{12}^2\mathfrak{G}_{22}\\+\mathfrak{A}_{12}\mathfrak{B}_{12}\mathfrak{D}_{22}+\mathfrak{A}_{12}\mathfrak{B}_{22}\mathfrak{D}_{12}-2\mathfrak{A}_{12}\mathfrak{D}_{12}\mathfrak{D}_{22}-\mathfrak{A}_{22}\mathfrak{B}_{12}\mathfrak{D}_{12}+\mathfrak{A}_{22}\mathfrak{D}_{12}^2\end{pmatrix}}{\mathfrak{A}_{11}\mathfrak{A}_{22}-\mathfrak{A}_{12}^2},
\tag{34 g}
$$

$$
\begin{aligned}
\mathfrak{H}_{22}&=\frac{\mathfrak{A}_{11}\mathfrak{B}_{22}-\mathfrak{A}_{11}\mathfrak{D}_{22}-\mathfrak{A}_{12}\mathfrak{B}_{12}+2\mathfrak{A}_{12}\mathfrak{D}_{12}-\mathfrak{A}_{22}\mathfrak{D}_{11}}{\mathfrak{A}_{11}\mathfrak{A}_{22}-\mathfrak{A}_{12}^2}-\frac{2\mathfrak{B}_{66}}{\mathfrak{A}_{66}}\\
&\quad+\frac{2\mathfrak{D}_{66}}{\mathfrak{A}_{66}},
\end{aligned}
\tag{34b}
$$

$$\mathfrak{H}_{28} = -\frac{\begin{pmatrix} \mathfrak{A}_{11}\mathfrak{B}_{22}\mathfrak{D}_{12} - 2\mathfrak{A}_{11}\mathfrak{D}_{12}\mathfrak{D}_{22} - \mathfrak{A}_{12}\mathfrak{B}_{12}\mathfrak{D}_{12} - \mathfrak{A}_{12}\mathfrak{B}_{22}\mathfrak{D}_{11} \\ +2\mathfrak{A}_{12}\mathfrak{D}_{11}\mathfrak{D}_{22} + 2\mathfrak{A}_{12}\mathfrak{D}_{12}^2 + \mathfrak{A}_{22}\mathfrak{B}_{12}\mathfrak{D}_{11} - 2\mathfrak{A}_{22}\mathfrak{D}_{11}\mathfrak{D}_{12} \end{pmatrix}}{\mathfrak{A}_{11}\mathfrak{A}_{22} - \mathfrak{A}_{12}^2}, \\ -4\frac{\mathfrak{D}_{66}(\mathfrak{B}_{66} - \mathfrak{D}_{66})}{\mathfrak{A}_{66}} - 4\mathfrak{G}_{66} - 2\mathfrak{G}_{12} + 4\mathfrak{E}_{66} + \mathfrak{E}_{12} \tag{34h}$$

$$\mathfrak{H}_{29} = \mathfrak{A}_{44} + E_{44} + 2C_{44}, \mathfrak{H}_{30} = \mathfrak{E}_{55} + \mathfrak{C}_{55}, \tag{34i}$$

$$\mathfrak{H}_{31} = -\frac{\begin{pmatrix} \mathfrak{A}_{11}\mathfrak{A}_{22}\mathfrak{E}_{11} - \mathfrak{A}_{11}\mathfrak{A}_{22}\mathfrak{G}_{11} - \mathfrak{A}_{11}\mathfrak{B}_{12}\mathfrak{D}_{12} + \mathfrak{A}_{11}\mathfrak{D}_{12}^2 - \mathfrak{A}_{12}^2\mathfrak{E}_{11} + \mathfrak{A}_{12}^2\mathfrak{G}_{11} \\ +\mathfrak{A}_{12}\mathfrak{B}_{11}\mathfrak{D}_{12} + \mathfrak{A}_{12}\mathfrak{B}_{12}\mathfrak{D}_{11} - 2\mathfrak{A}_{12}\mathfrak{D}_{11}\mathfrak{D}_{12} - \mathfrak{A}_{22}\mathfrak{B}_{11}\mathfrak{D}_{11} + \mathfrak{A}_{22}\mathfrak{D}_{11}^2 \end{pmatrix}}{\mathfrak{A}_{11}\mathfrak{A}_{22} - \mathfrak{A}_{12}^2}, \tag{34j}$$

$$\mathfrak{H}_{32} = -\frac{\begin{pmatrix} \mathfrak{A}_{11}\mathfrak{A}_{22}\mathfrak{E}_{22} - \mathfrak{A}_{11}\mathfrak{A}_{22}\mathfrak{G}_{22} - \mathfrak{A}_{11}\mathfrak{B}_{22}\mathfrak{D}_{22} + \mathfrak{A}_{11}\mathfrak{D}_{22}^2 - \mathfrak{A}_{12}^2\mathfrak{E}_{22} + \mathfrak{A}_{12}^2\mathfrak{G}_{22} \\ +\mathfrak{A}_{12}\mathfrak{B}_{12}\mathfrak{D}_{22} + \mathfrak{A}_{12}\mathfrak{B}_{22}\mathfrak{D}_{12} - 2\mathfrak{A}_{12}\mathfrak{D}_{12}\mathfrak{D}_{22} - \mathfrak{A}_{22}\mathfrak{B}_{12}\mathfrak{D}_{12} + \mathfrak{A}_{22}\mathfrak{D}_{12}^2 \end{pmatrix}}{\mathfrak{A}_{11}\mathfrak{A}_{22} - \mathfrak{A}_{12}^2}, \tag{34k}$$

$$\mathfrak{H}_{33} = -\frac{\begin{pmatrix} 2\mathfrak{A}_{11}\mathfrak{A}_{22}\mathfrak{A}_{66}\mathfrak{E}_{12} + 4\mathfrak{A}_{11}\mathfrak{A}_{22}\mathfrak{A}_{66}\mathfrak{E}_{66} - 2\mathfrak{A}_{11}\mathfrak{A}_{22}\mathfrak{A}_{66}\mathfrak{G}_{12} - 4\mathfrak{A}_{11}\mathfrak{A}_{22}\mathfrak{A}_{66}\mathfrak{G}_{66} \\ +4\mathfrak{A}_{11}\mathfrak{A}_{22}\mathfrak{D}_{66}^2 - 4\mathfrak{A}_{11}\mathfrak{A}_{22}\mathfrak{B}_{66}\mathfrak{D}_{66} - \mathfrak{A}_{11}\mathfrak{A}_{66}\mathfrak{B}_{12}\mathfrak{D}_{22} - \mathfrak{A}_{11}\mathfrak{A}_{66}\mathfrak{B}_{22}\mathfrak{D}_{12} \\ +2\mathfrak{A}_{11}\mathfrak{A}_{66}\mathfrak{D}_{12}\mathfrak{D}_{22} - 2\mathfrak{A}_{12}^2\mathfrak{A}_{66}\mathfrak{E}_{12} - 4\mathfrak{A}_{12}^2\mathfrak{A}_{66}\mathfrak{E}_{66} + 2\mathfrak{A}_{12}^2\mathfrak{A}_{66}\mathfrak{G}_{12} + 4\mathfrak{A}_{12}^2\mathfrak{A}_{66}\mathfrak{G}_{66} \\ +4\mathfrak{A}_{12}^2\mathfrak{B}_{66}\mathfrak{D}_{66} - 4\mathfrak{A}_{12}^2\mathfrak{D}_{66}^2 + \mathfrak{A}_{12}\mathfrak{A}_{66}\mathfrak{B}_{11}\mathfrak{D}_{22} + 2\mathfrak{A}_{12}\mathfrak{A}_{66}\mathfrak{B}_{12}\mathfrak{D}_{12} + \mathfrak{A}_{12}\mathfrak{A}_{66}\mathfrak{B}_{22}\mathfrak{D}_{11} \\ -2\mathfrak{A}_{12}\mathfrak{A}_{66}\mathfrak{D}_{11}\mathfrak{D}_{22} - 2\mathfrak{A}_{12}\mathfrak{A}_{66}\mathfrak{D}_{12}^2 - \mathfrak{A}_{22}\mathfrak{A}_{66}\mathfrak{B}_{11}\mathfrak{D}_{12} - \mathfrak{A}_{22}\mathfrak{A}_{66}\mathfrak{B}_{12}\mathfrak{D}_{11} + 2\mathfrak{A}_{22}\mathfrak{A}_{66}\mathfrak{D}_{11}\mathfrak{D}_{12} \end{pmatrix}}{\mathfrak{A}_{66}\left(\mathfrak{A}_{11}\mathfrak{A}_{22} - \mathfrak{A}_{12}^2\right)}, \tag{34l}$$

$$\mathfrak{H}_{34} = \frac{\mathfrak{A}_{11}\mathfrak{A}_{22}\mathfrak{G}_{11} - \mathfrak{A}_{11}\mathfrak{D}_{12}^2 - \mathfrak{A}_{12}^2\mathfrak{G}_{11} + 2\mathfrak{A}_{12}\mathfrak{D}_{11}\mathfrak{D}_{12} - \mathfrak{A}_{22}\mathfrak{D}_{11}^2}{\mathfrak{A}_{11}\mathfrak{A}_{22} - \mathfrak{A}_{12}^2}, \tag{34m}$$

$$\mathfrak{H}_{35} = \frac{\mathfrak{A}_{11}\mathfrak{A}_{22}\mathfrak{G}_{22} - \mathfrak{A}_{11}\mathfrak{D}_{22}^2 - \mathfrak{A}_{12}^2\mathfrak{G}_{22} + 2\mathfrak{A}_{12}\mathfrak{D}_{11}\mathfrak{D}_{22} - \mathfrak{A}_{22}\mathfrak{D}_{11}^2}{\mathfrak{A}_{11}\mathfrak{A}_{22} - \mathfrak{A}_{12}^2}, \tag{34n}$$

$$\mathfrak{H}_{36} = \frac{2\begin{pmatrix} \mathfrak{A}_{11}\mathfrak{A}_{22}\mathfrak{A}_{66}\mathfrak{G}_{12} + 2\mathfrak{A}_{11}\mathfrak{A}_{22}\mathfrak{A}_{66}\mathfrak{G}_{66} - 2\mathfrak{A}_{11}\mathfrak{A}_{22}\mathfrak{D}_{66}^2 - \mathfrak{A}_{11}\mathfrak{A}_{66}\mathfrak{D}_{12}\mathfrak{D}_{22} - \mathfrak{A}_{12}^2\mathfrak{A}_{66}\mathfrak{G}_{12} \\ -2\mathfrak{A}_{12}^2\mathfrak{A}_{66}\mathfrak{G}_{66} + 2\mathfrak{A}_{12}^2\mathfrak{D}_{66}^2 + \mathfrak{A}_{12}\mathfrak{A}_{66}\mathfrak{D}_{11}\mathfrak{D}_{22} + \mathfrak{A}_{12}\mathfrak{A}_{66}\mathfrak{D}_{12}^2 - \mathfrak{A}_{22}\mathfrak{A}_{66}\mathfrak{D}_{11}\mathfrak{D}_{12} \end{pmatrix}}{\left(\mathfrak{A}_{11}\mathfrak{A}_{22} - \mathfrak{A}_{12}^2\right)\mathfrak{A}_{66}}, \tag{34o}$$

$$\mathfrak{H}_{37} = -2\mathfrak{C}_{44} - \mathfrak{E}_{44} - \mathfrak{A}_{44}, \mathfrak{H}_{38} = -\mathfrak{E}_{55} - \mathfrak{C}_{55}. \tag{34p}$$

3.4. Solutions

The Galerkin method, a numerical technique used to discover solutions for partial differential equations (the motion equations) together with SSSS BCs, may be used to determine the approximate solution for double-curved shallow shells. Using this method, a suitable collection of basic functions is chosen, and coefficients are then found in order to describe the answer as a linear combination of these basic functions. The partial differential equation is transformed into an algebraic system of equations as a consequence of this procedure. The boundary condition can be shown as follows:

$$\begin{array}{l} \mathscr{u}_0 = \mathscr{v}_0 = \mathscr{w}_{,\mathscr{Y}} = \mathfrak{Y}_{,\mathscr{Y}} = \mathbb{m}_{\mathscr{X}\mathscr{Y}} = 0, \mathbb{m}_{\mathscr{X}} = \mathbb{m}_{\mathscr{X}0} \text{ at } X = 0, a \\ \mathscr{w}_0 = \mathscr{u}_0 = \mathscr{w}_{,\mathscr{X}} = \mathfrak{Y}_{,\mathscr{X}} = \mathbb{m}_{\mathscr{X}\mathscr{Y}} = 0, \mathbb{m}_{\mathscr{Y}} = \mathbb{m}_{\mathscr{Y}0} \text{ at } Y = 0, b \end{array} \tag{35}$$

The approximate solution of the double curved shallow shells satisfied SSSS can be sought as:

$$\mathscr{u}_0(\mathscr{X}, \mathscr{Y}, t) = \mathscr{U}(t)\cos(\lambda_m \mathscr{X})\sin(\delta_n \mathscr{Y}), \tag{36}$$

$$\mathscr{v}_0(\mathscr{X}, \mathscr{Y}, t) = \mathscr{V}(t)\sin(\lambda_m \mathscr{X})\cos(\delta_n \mathscr{Y}),$$

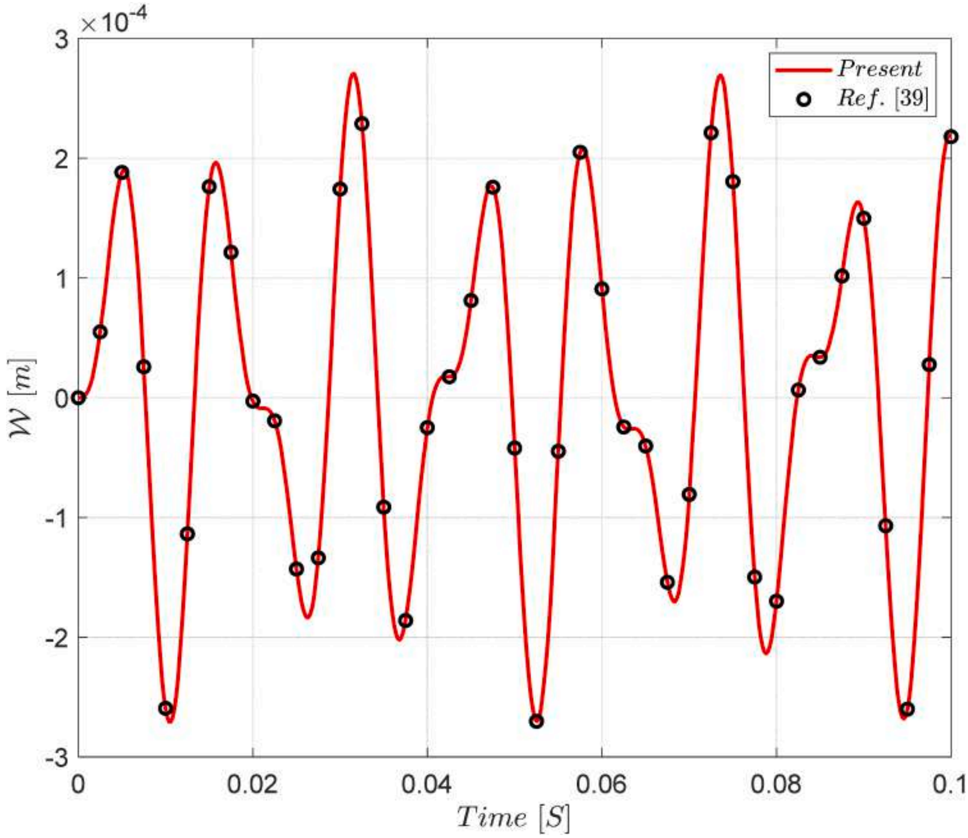

Fig. 3. Comparison between the present study and Ref. [40] of the FG-GPLRC plate with $q(t) = 2000\sin(450t)$, $GPL-UD$, $\mathscr{W}_{GPL} = 0.3$ $[wt\%]$, $a/h = 20$, and $b = a$.

$$w(\mathscr{X},\mathscr{Y},t) = \mathscr{W}(t)\sin(\lambda_m\mathscr{X})\sin(\delta_n\mathscr{Y}),$$

$$\mathfrak{Y}(\mathscr{X},\mathscr{Y},t) = \mathfrak{L}(t)\sin(\lambda_m\mathscr{X})\sin(\delta_n\mathscr{Y}),$$

in which $\lambda_m = m\pi/a$, $\delta_n = n\pi/b$, and $\mathscr{U}(t)$, $\mathscr{V}(t)$, $\mathscr{W}(t), \mathfrak{L}(t)$ are time-dependent displacement and rotation amplitudes, respectively. The stress function $\mathscr{T}(\mathscr{X},\mathscr{Y},t)$ replaces the force and moment components in the equations of motion as a variable in the stress function technique. Satisfying the relevant BCs is necessary to determine the solution for $\mathscr{T}(\mathscr{X}, \mathscr{Y}, t)$. The geometrical compatibility equation in Eq. (29), moreover, determines the coefficients F_i in Eq. (37).

$$\mathscr{T}(\mathscr{X},\mathscr{Y},t) = F_1\cos2\lambda_m\mathscr{X} + F_2\cos2\delta_n\mathscr{Y} + F_3\sin\lambda_m\mathscr{X}\sin\delta_n\mathscr{Y} + \frac{1}{2}\mathbb{n}_{\mathscr{X}o}\mathscr{Y}^2 + \frac{1}{2}\mathbb{n}_{\mathscr{Y}o}\mathscr{X}^2, \tag{37}$$

in which $\mathbb{n}_{\mathscr{X}o}$ and $\mathbb{n}_{\mathscr{Y}o}$ represent the axial pre-stress along the $\mathscr{X}$ and $\mathscr{Y}$ axes, respectively.

$$F_1 = \frac{1}{32}\frac{\delta_n^2}{\lambda_m^2\mathfrak{H}_{11}}\mathscr{W}(t)^2,\ F_2 = \frac{1}{32}\frac{\lambda_m^2}{\delta_n^2\mathfrak{H}_{12}}\mathscr{W}(t)^2,\ F_3 = F_{31}\mathscr{W}(t) + F_{32}\mathfrak{L}(t), \tag{38a}$$

$$F_{31} = -\frac{(\mathfrak{H}_{14}\lambda_m^4 + \mathfrak{H}_{15}\delta_n^4 + \mathfrak{H}_{16}\delta_n^2\lambda_m^2)R_{\mathscr{X}}R_{\mathscr{Y}} - \lambda_m^2R_{\mathscr{X}} - \delta_n^2R_{\mathscr{Y}}}{(\mathfrak{H}_{11}\lambda_m^4 + \mathfrak{H}_{12}\delta_n^4 + \mathfrak{H}_{13}\lambda_m^2\delta_n^2)R_{\mathscr{X}}R_{\mathscr{Y}}}, \tag{38b}$$

$$F_{32} = -\frac{\mathfrak{H}_{17}\lambda_m^4 + \mathfrak{H}_{18}\delta_n^4 + \mathfrak{H}_{19}\delta_n^2\lambda_m^2}{\mathfrak{H}_{11}\lambda_m^4 + \mathfrak{H}_{12}\delta_n^4 + \mathfrak{H}_{13}\lambda_m^2\delta_n^2}. \tag{38c}$$

To get results, substitute solutions in Eqs. (36), (37) that correspond to SSSS BCs in Eqs. (33a), and (33b). Then, use the Galerkin method:

$$\left(\mathfrak{G}_1^1 + \mathfrak{G}_1^{11}\mathbb{n}_{\mathscr{X}0} + \mathfrak{G}_1^{12}\mathbb{n}_{\mathscr{Y}0}\right)\mathscr{W}(t) + \mathfrak{G}_1^2\mathscr{W}(t)^2 + \mathfrak{G}_1^3\mathscr{W}(t)^3 + \mathfrak{G}_1^4\mathfrak{L}(t) + \mathfrak{G}_1^5\mathscr{W}(t)\mathfrak{L}(t) + \mathfrak{G}_1^6\left(\frac{\mathbb{n}_{\mathscr{X}0}}{R_{\mathscr{X}}} + \frac{\mathbb{n}_{\mathscr{Y}0}}{R_{\mathscr{Y}}} + q\right) = \overline{J}_1^1\frac{\partial^2\mathscr{W}(t)}{\partial t^2} + \overline{J}_1^2\frac{\partial^2\mathfrak{L}(t)}{\partial t^2}, \tag{39a}$$

$$\mathfrak{G}_2^1\mathscr{W}(t) + \mathfrak{G}_2^2\mathscr{W}(t)^2 + \mathfrak{G}_2^3\mathfrak{L}(t) = \overline{J}_2^1\frac{\partial^2\mathscr{W}(t)}{\partial t^2} + \overline{J}_2^2\frac{\partial^2\mathfrak{L}(t)}{\partial t^2}. \tag{39b}$$

where $\mathfrak{G}_i^j(i = 1\text{to}2, j = 1\text{to}12); \overline{J}_i^j(i = 1\text{to}2, j = 1\text{to}2)$ for three cases of SSSS BCs are given in Eqs. (40a)-(40l).

$$\mathfrak{G}_1^1 = \frac{\begin{pmatrix} F_{31}m^4\pi^4\mathfrak{H}_{17}b^4 + n^4\pi^4F_{31}\mathfrak{H}_{21}a^4 + F_{31}\mathfrak{H}_{22}m^2\pi^4n^2b^2a^2 + \pi^4\mathfrak{H}_{23}m^4b^4 \\ +n^4\pi^4\mathfrak{H}_{24}a^4 + n^2\pi^4\mathfrak{H}_{25}m^2b^2a^2 - \pi^2\mathfrak{H}_{29}m^2b^4a^2 - n^2\pi^2\mathfrak{H}_{30}b^2a^4 \end{pmatrix}}{4b^3a^3} - \frac{1}{4}ba\mathbb{k}_1 + \frac{\left(-\pi^2a^4b^2n^2 - \pi^2a^2b^4m^2\right)\mathbb{k}_2}{4b^3a^3} - \frac{\pi^2F_{31}m^2b}{4aR_{\mathscr{Y}}} - \frac{F_{31}n^2\pi^2a}{4bR_{\mathscr{X}}}, \tag{40a}$$

$$\mathfrak{G}_1^{11} = -\frac{m^2\pi^2b}{4a},\ \mathfrak{G}_1^{12} = -\frac{n^2\pi^2a}{4b}, \tag{40b}$$

$$\mathfrak{G}_1^2 = \frac{1}{6}\left\{\frac{16F_{31}\mathfrak{H}_{11}\mathfrak{H}_{12}\pi^2m^2n^2 - 4\mathfrak{H}_{11}\mathfrak{H}_{21}\pi^2m^2n^2 - 4\mathfrak{H}_{12}\mathfrak{H}_{17}\pi^2m^2n^2}{ba\mathfrak{H}_{11}\mathfrak{H}_{12}nm} + \frac{an}{b\mathfrak{H}_{11}mR_{\mathscr{Y}}} + \frac{bm}{a\mathfrak{H}_{12}nR_{\mathscr{X}}}\right\}, \tag{40c}$$

$$\mathfrak{G}_1^3 = -\frac{1}{64}\frac{\pi^4\left(\mathfrak{H}_{11}b^4m^4 + \mathfrak{H}_{12}a^4n^4\right)}{b^3a^3\mathfrak{H}_{11}\mathfrak{H}_{12}},\ \mathfrak{G}_1^5 = \frac{8}{3}\frac{F_{32}mn\pi^2}{ab},\ \mathfrak{G}_1^6 = \frac{4ab}{mn\pi^2}, \tag{40d}$$

$$\mathfrak{G}_1^4 = \frac{\pi^2\begin{pmatrix} F_{32}\mathfrak{H}_{17}\pi^2b^4m^4 + F_{32}\mathfrak{H}_{21}\pi^2a^4n^4 + F_{32}\mathfrak{H}_{22}\pi^2a^2b^2m^2n^2 + \mathfrak{H}_{26}\pi^2b^4m^4 \\ +\mathfrak{H}_{27}\pi^2a^4n^4 + \mathfrak{H}_{28}\pi^2a^2b^2m^2n^2 - \mathfrak{H}_{29}a^2b^4m^2 - \mathfrak{H}_{30}a^4b^2n^2 \end{pmatrix}}{4b^3a^3} - \frac{\pi^2F_{32}m^2b}{4aR_{\mathscr{Y}}} - \frac{\pi^2n^2F_{32}a}{4bR_{\mathscr{X}}}, \tag{40e}$$

$$\mathfrak{G}_2^1 = -\frac{1}{4}\frac{\pi^2\begin{pmatrix} F_{31}\mathfrak{H}_{17}\pi^2b^4m^4 + F_{31}\mathfrak{H}_{18}\pi^2a^4n^4 + F_{31}\mathfrak{H}_{19}\pi^2a^2b^2m^2n^2 - \mathfrak{H}_{31}\pi^2b^4m^4 \\ -\mathfrak{H}_{32}\pi^2a^4n^4 - \mathfrak{H}_{33}\pi^2a^2b^2m^2n^2 + \mathfrak{H}_{37}m^2b^4a^2 + n^2\mathfrak{H}_{38}b^2a^4 \end{pmatrix}}{a^3b^3}, \tag{40f}$$

$$\mathfrak{G}_2^2 = \frac{2}{3}\frac{\pi^2mn(\mathfrak{H}_{11}\mathfrak{H}_{18} + \mathfrak{H}_{12}\mathfrak{H}_{17})}{ab\mathfrak{H}_{12}\mathfrak{H}_{11}}, \tag{40 g}$$

$$\mathfrak{G}_2^3 = -\frac{1}{4}\frac{\pi^2\begin{pmatrix} F_{32}\mathfrak{H}_{17}\pi^2b^4m^4 + F_{32}\mathfrak{H}_{18}\pi^2a^4n^4 + F_{32}\mathfrak{H}_{19}\pi^2a^2b^2m^2n^2 - \mathfrak{H}_{34}\pi^2b^4m^4 \\ -\mathfrak{H}_{35}\pi^2a^4n^4 - \mathfrak{H}_{36}\pi^2a^2b^2m^2n^2 + \mathfrak{H}_{37}a^2b^4m^2 + \mathfrak{H}_{38}a^4b^2n^2 \end{pmatrix}}{a^3b^3}, \tag{40h}$$

$$\overline{J_1^1} = \frac{1}{4}\frac{\begin{pmatrix} \mathscr{L}_0\mathscr{L}_2\pi^2a^2n^2 + \mathscr{L}_0\mathscr{L}_2\pi^2b^2m^2 - 2\mathscr{L}_0J_2\pi^2a^2n^2 - 2\mathscr{L}_0J_2\pi^2b^2m^2 \\ +\mathscr{L}_0J_3\pi^2a^2n^2 + \mathscr{L}_0J_3\pi^2b^2m^2 - \mathscr{L}_1^2\pi^2a^2n^2 - \mathscr{L}_1^2\pi^2b^2m^2 \\ +2\mathscr{L}_1J_1\pi^2a^2n^2 + 2\mathscr{L}_1J_1\pi^2b^2m^2 - J_1^2\pi^2a^2n^2 - J_1^2\pi^2b^2m^2 + \mathscr{L}_0^2b^2a^2 \end{pmatrix}}{ba\mathscr{L}_0}, \tag{40i}$$

$$\overline{J_1^2} = -\frac{1}{4}\frac{\pi^2\begin{pmatrix} \mathscr{L}_0J_2a^2n^2 + \mathscr{L}_0J_2b^2m^2 - \mathscr{L}_0J_3a^2n^2 - \mathscr{L}_0J_3b^2m^2 \\ -\mathscr{L}_1J_1a^2n^2 - \mathscr{L}_1J_1b^2m^2 + J_1^2a^2n^2 + J_1^2b^2m^2 \end{pmatrix}}{ba\mathscr{L}_0}, \tag{40j}$$

$$\overline{J_2^1} = \frac{1}{4}\frac{\pi^2\begin{pmatrix} \mathscr{L}_0J_2a^2n^2 + \mathscr{L}_0J_2b^2m^2 - \mathscr{L}_0J_3a^2n^2 - \mathscr{L}_0J_3b^2m^2 \\ -\mathscr{L}_1J_1a^2n^2 - \mathscr{L}_1J_1b^2m^2 + J_1^2a^2n^2 + J_1^2b^2m^2 \end{pmatrix}}{ab\mathscr{L}_0}, \tag{40k}$$

$$\overline{J_2^2} = -\frac{1}{4}\frac{\pi^2\left(\mathscr{L}_0J_3a^2n^2 + \mathscr{L}_0J_3b^2m^2 - J_1^2a^2n^2 - J_1^2b^2m^2\right)}{ab\mathscr{L}_0}. \tag{40l}$$

4. Nonlinear dynamic response analysis

The fourth-order Runge–Kutta technique may be used to solve a series of second-order nonlinear differential equations in order to determine the nonlinear dynamic response:

$$\overline{J_1^1}\frac{\partial^2\mathscr{W}(t)}{\partial t^2} + \overline{J_1^2}\frac{\partial^2\mathfrak{L}(t)}{\partial t^2} = \left(\mathfrak{G}_1^1 + \mathfrak{G}_1^{11}\mathfrak{m}_{\mathscr{X}0} + \mathfrak{G}_1^{11}\mathfrak{m}_{\mathscr{Y}0}\right)\mathscr{W}(t) + \mathfrak{G}_1^2\mathscr{W}(t)^2 + \mathfrak{G}_1^3\mathscr{W}(t)^3 + \mathfrak{G}_1^4\mathfrak{L}(t) + \mathfrak{G}_1^5\mathscr{W}(t)\mathfrak{L}(t) + \mathfrak{G}_1^6\left(\frac{\mathfrak{m}_{\mathscr{X}0}}{R_{\mathscr{X}}} + \frac{\mathfrak{m}_{\mathscr{Y}0}}{R_{\mathscr{Y}}} + q(t)\right), \tag{41a}$$

$$\overline{J_2^1}\frac{\partial^2\mathscr{W}(t)}{\partial t^2} + \overline{J_2^2}\frac{\partial^2\mathfrak{L}(t)}{\partial t^2} = \mathfrak{G}_2^1\mathscr{W}(t) + \mathfrak{G}_2^2\mathscr{W}(t)^2 + \mathfrak{G}_2^3\mathfrak{L}(t). \tag{41b}$$

These equations could be solved by using the fourth – order Runge – Kutta method with the initial conditions are chosen as $\mathscr{W}(0) = 0$, $\mathfrak{L}(0) = 0$ and $\frac{d\mathscr{W}}{dt}(0) = 0$, $\frac{d\mathfrak{L}}{dt}(0) = 0$.

5. An introduction on SVM-DNN-RF algorithm to predict nonlinear dynamic information of the composite structures using appropriate dataset of mathematics simulation

Machine learning (ML) is a field of study in artificial intelligence concerned with the development and study of statistical algorithms that can learn from data and generalize to unseen data, and thus perform

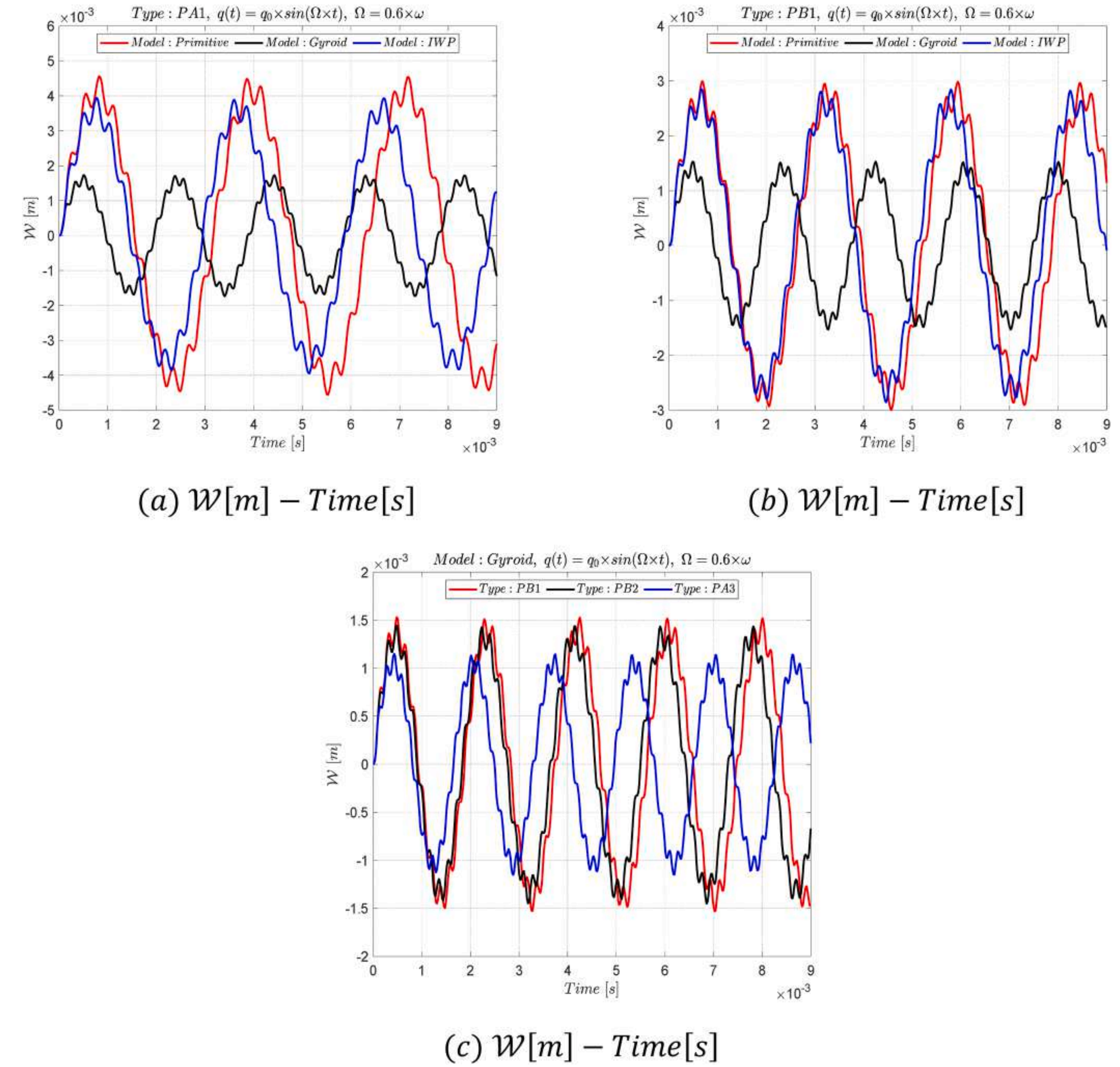

Fig. 4. The influence of various TPMS models on the dynamic deflection of the TPMS doubly curved panel under frequency excitation at various times.

tasks without explicit instructions [38]. The SVM-DNN-RF algorithm is an advanced hybrid machine learning approach that integrates Support Vector Machines (SVM), Deep Neural Networks (DNN), and Random Forest (RF) to predict the nonlinear dynamic behavior of composite structures. Composite materials, due to their complex anisotropic and heterogeneous nature, exhibit nonlinear dynamic responses that are challenging to model using traditional methods. By combining these three powerful techniques, the SVM-DNN-RF algorithm leverages the strengths of each model to capture intricate relationships between input features and the dynamic response of the structure, making it ideal for predicting complex behaviors such as vibration, stress distribution, and failure modes. SVM is effective in handling high-dimensional, non-linear data, offering robust classification and regression capabilities. DNN, on the other hand, excels at learning intricate patterns and dependencies from large datasets, particularly when there is limited prior knowledge about the structure's behavior. Random Forest adds an ensemble learning approach, combining multiple decision trees to improve prediction accuracy and reduce overfitting, thus providing a more generalized model. When applied to a dataset generated through mathematical simulations of composite structures under dynamic loading conditions, this hybrid model can accurately predict the nonlinear responses of these materials under a wide range of scenarios [39]. The appropriate dataset for this model consists of simulated data that captures various dynamic characteristics of composite structures, including material properties, geometric configurations, boundary conditions, and loading types. By training the SVM-DNN-RF model on this data, engineers can gain valuable insights into the performance and failure mechanisms of composite materials without the need for expensive and time-consuming physical testing. This approach provides a powerful tool for the design and optimization of composite structures, ensuring their reliability and efficiency in real-world applications such as aerospace, automotive, and civil engineering.

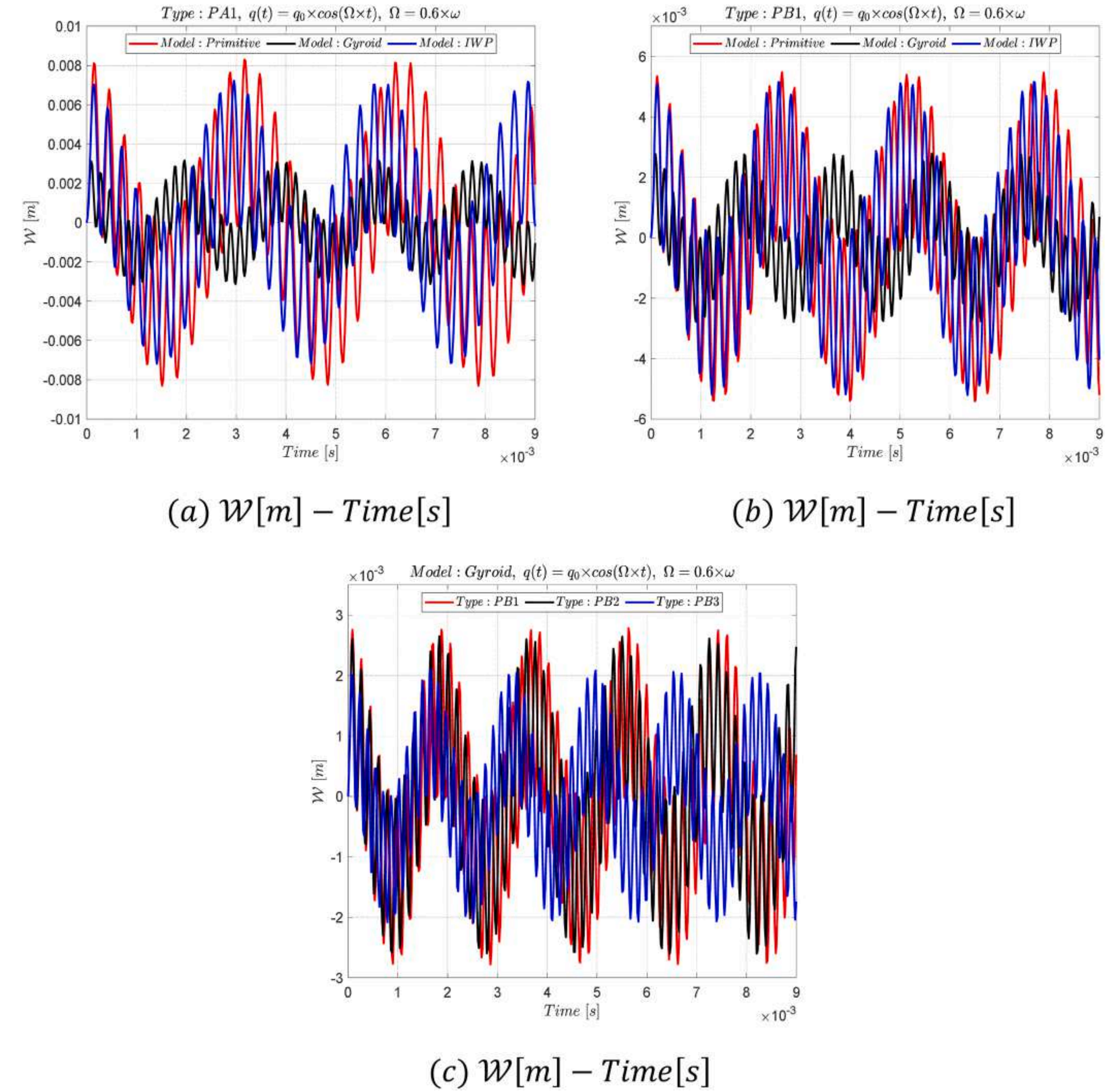

Fig. 5. The influence of various TPMS types on the dynamic deflection of the TPMS doubly curved panel under frequency excitation at various times.

The SVM-DNN-RF algorithm offers several key advantages over traditional machine learning algorithms when predicting the nonlinear dynamic behavior of composite structures:

1. **Enhanced Accuracy**: By combining Support Vector Machines (SVM), Deep Neural Networks (DNN), and Random Forest (RF), the algorithm benefits from the strengths of each individual model, leading to more accurate predictions than using any of these methods alone. SVM handles high-dimensional data effectively, DNN captures complex non-linear patterns, and RF reduces overfitting and enhances generalization.
2. **Better Handling of Non-Linearity**: Composite structures often exhibit highly nonlinear dynamic behavior due to their complex material properties and geometries. The hybrid approach of SVM-DNN-RF excels in capturing these nonlinearities, which may be difficult for other algorithms like linear regression or basic decision trees to model accurately.
3. **Robustness to Overfitting**: The Random Forest component helps in reducing overfitting by averaging the results of multiple decision trees, which is a common issue when using deep neural networks or support vector machines independently. This feature ensures that the model generalizes better to new, unseen data.
4. **Adaptability to Complex Data**: The algorithm is particularly well-suited to work with large and complex datasets generated from mathematical simulations, which may include various dynamic conditions, material properties, and structural configurations. DNN excels at learning intricate patterns in these large

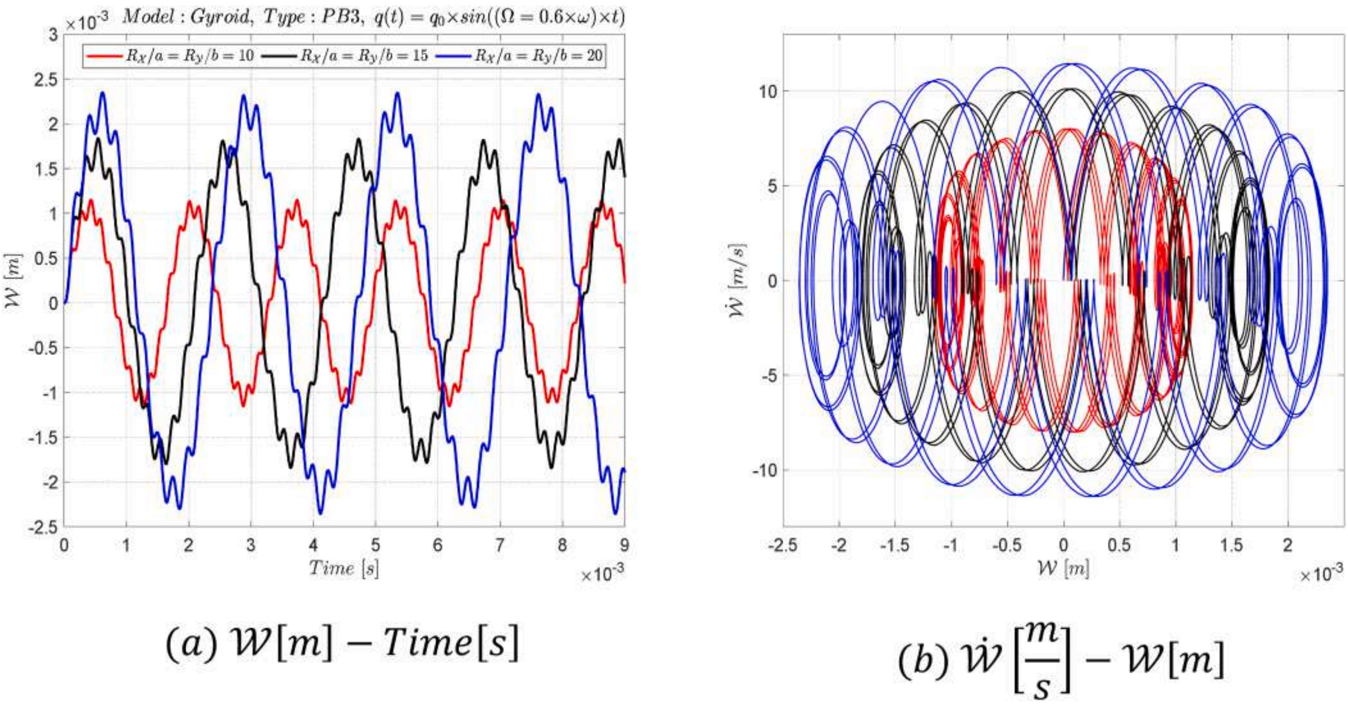

Fig. 6. The influence of various TPMS types on the $\mathcal{W} - Time$ and $\dot{\mathcal{W}} - \mathcal{W}$ curves of the TPMS doubly curved panel under frequency excitation.

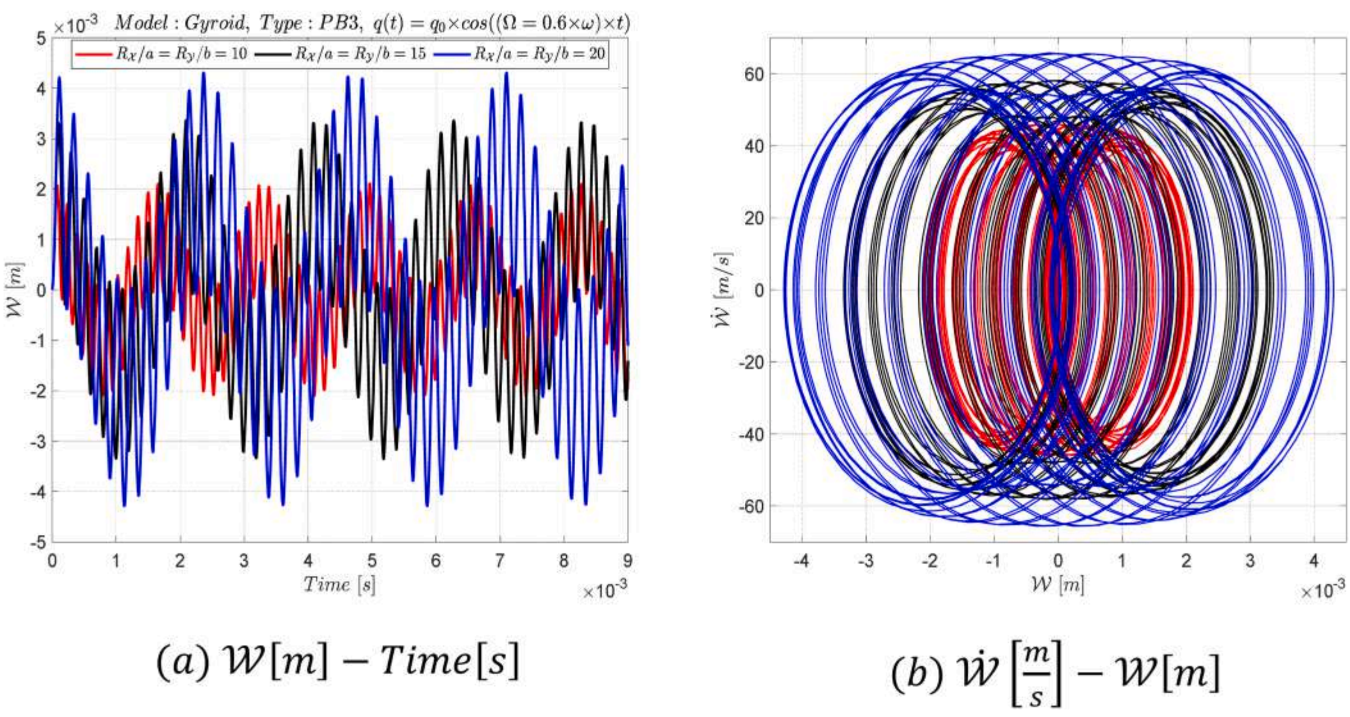

Fig. 7. The influence of various radius curvature factors on the $\mathcal{W} - Time$ and $\dot{\mathcal{W}} - \mathcal{W}$ curves of the TPMS doubly curved panel under frequency excitation.

datasets, providing insights into dynamic behaviors that might be overlooked by simpler algorithms.

5. **Flexibility**: The SVM-DNN-RF model can handle different types of input data, including both continuous and categorical features. This flexibility allows engineers to incorporate various parameters such as material properties, loading conditions, and geometrical configurations, ensuring comprehensive modeling of the system.
6. **Improved Efficiency**: Compared to other machine learning methods that might require extensive feature engineering or manual intervention, the hybrid model automatically learns the most relevant patterns from the data, reducing the need for domain-specific knowledge and saving time in the modeling process.
7. **Scalability**: The algorithm is highly scalable, meaning it can be applied to both small and large datasets effectively. This makes it

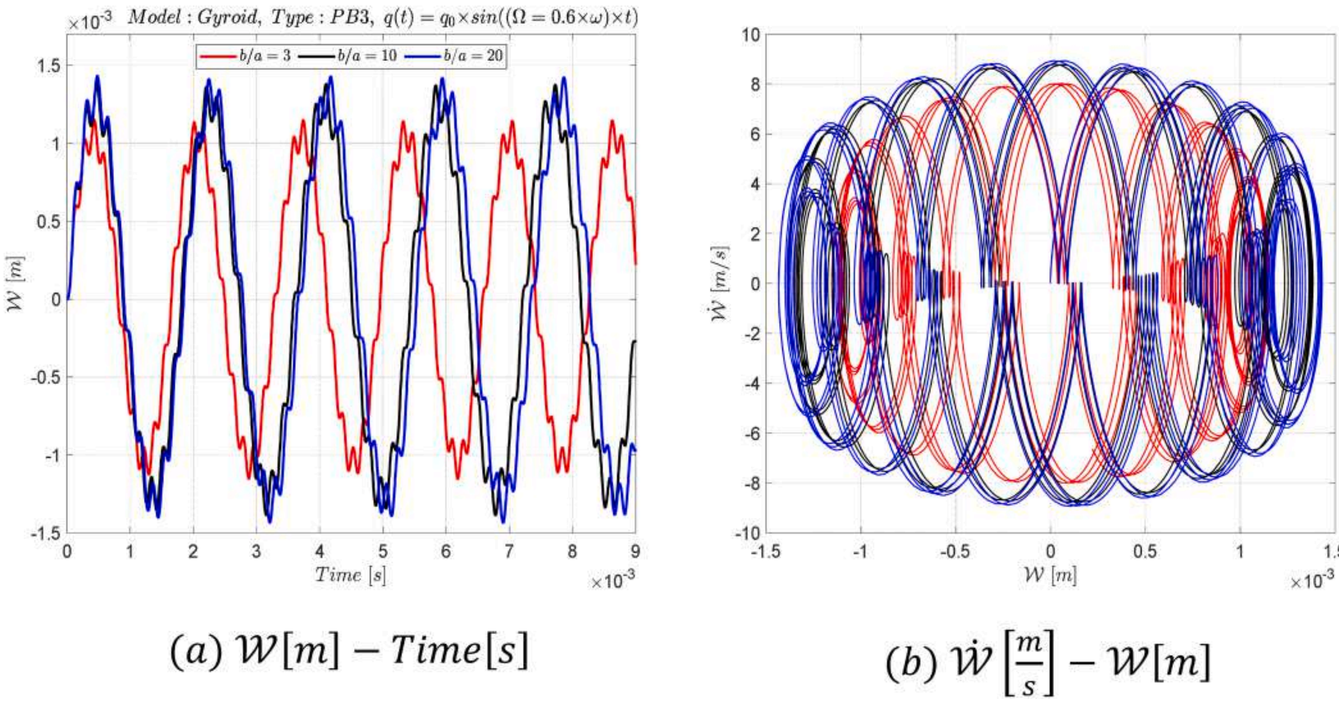

Fig. 8. The influence of various b/a ratios on the $\mathscr{W}$ – *Time* and $\dot{\mathscr{W}}$ – $\mathscr{W}$ curves of the TPMS doubly curved panel considering first pattern of frequency excitations.

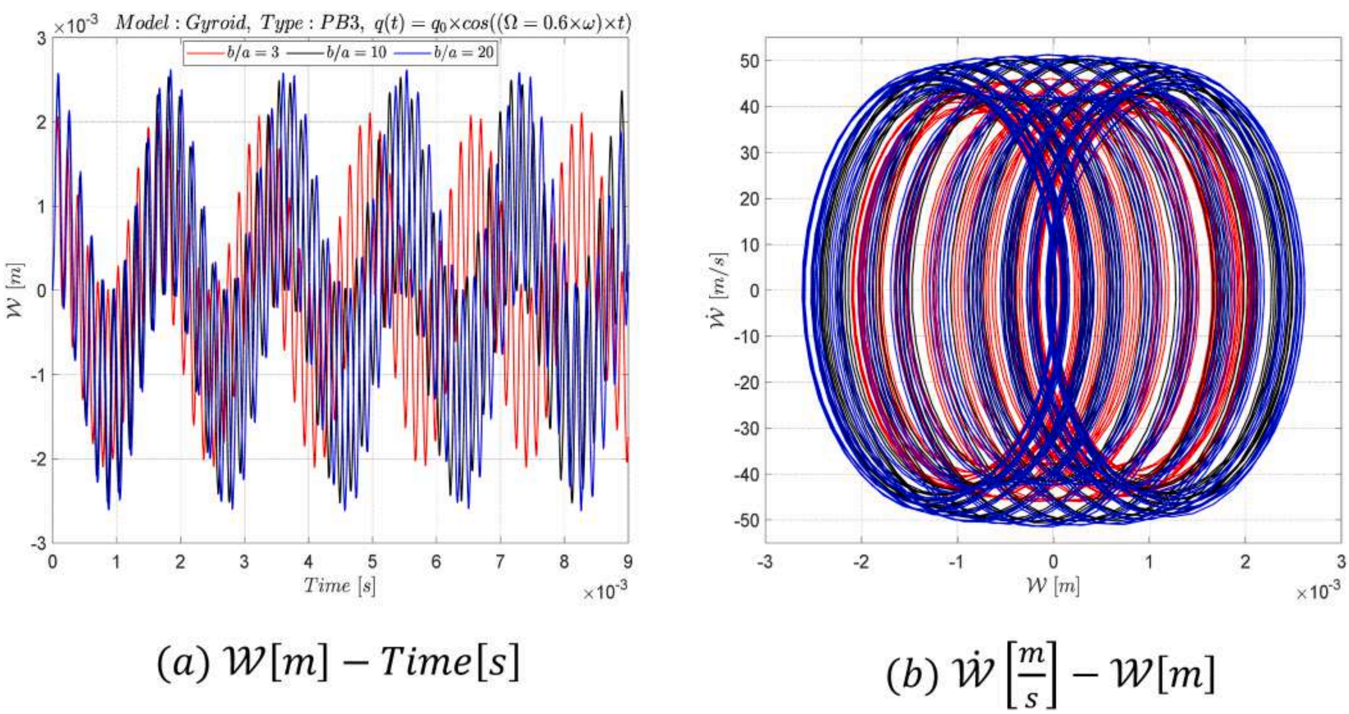

Fig. 9. The influence of various b/a ratios on the $\mathscr{W}$ – *Time* and $\dot{\mathscr{W}}$ – $\mathscr{W}$ curves of the TPMS doubly curved panel considering second pattern of frequency excitations.

suitable for a wide range of engineering applications, from small-scale simulations to large-scale systems with high-dimensional data.

8. **Multi-Model Integration**: The combination of three models (SVM, DNN, and RF) in a single framework allows for a more comprehensive understanding of the system's behavior, especially in cases where no single model is sufficient. This multi-model approach ensures a balanced performance across various types of data and prediction tasks.
9. **Robust to Noisy Data:** The algorithm's ensemble nature, particularly through the Random Forest component, helps it perform well even when the data is noisy or contains outliers, which is common in real-world simulations of composite structures.

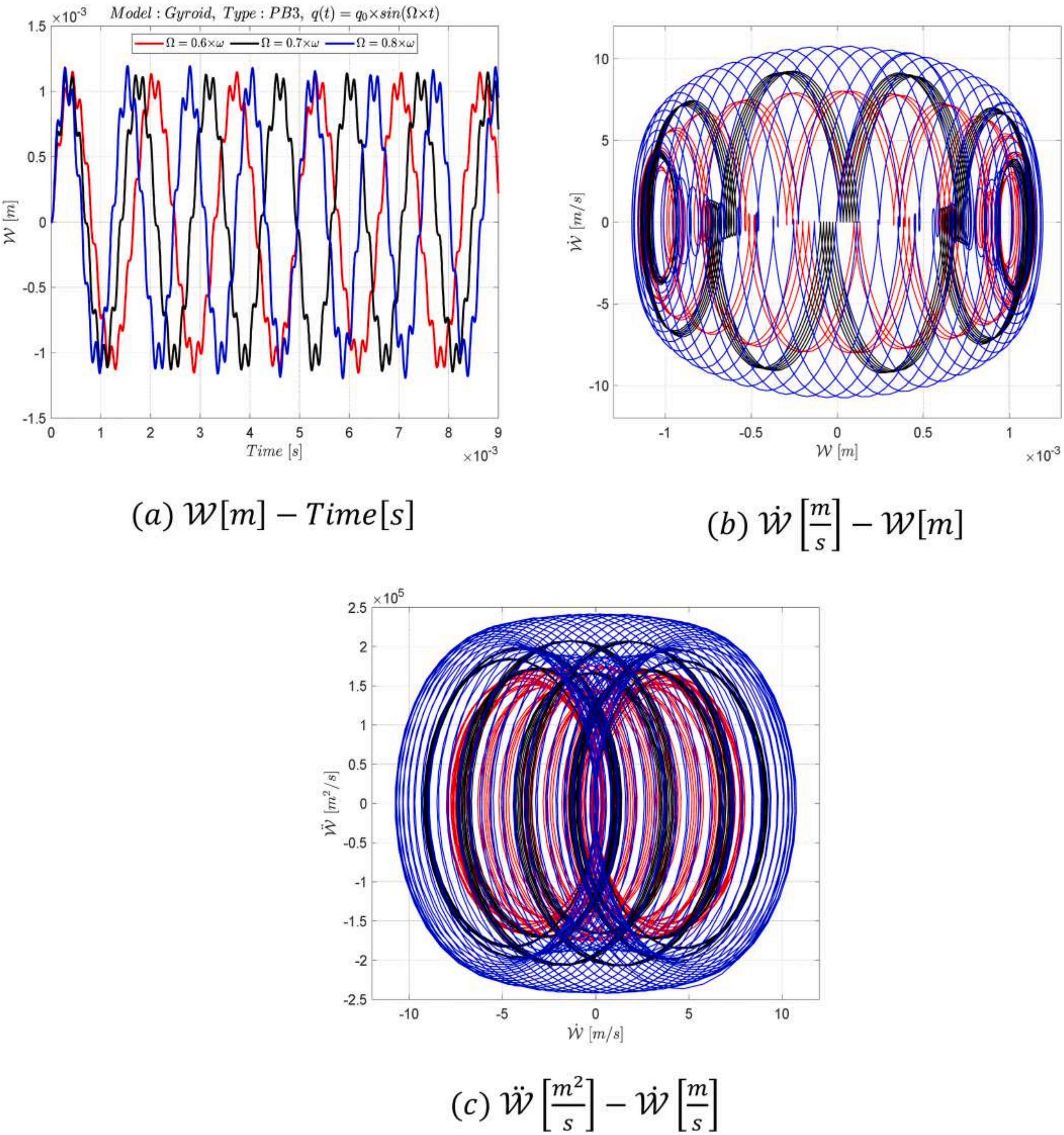

Fig. 10. The influence of various excitation frequencies on the $\mathscr{W}$ − *Time* and $\dot{\mathscr{W}} - \mathscr{W}$ and $\ddot{\mathscr{W}} - \dot{\mathscr{W}}$ curves of the TPMS doubly curved panel.

10. **Improved Interpretability:** Although deep learning models can often be seen as "black boxes," the integration with Random Forest allows for better interpretability of the results, helping engineers understand the influence of different features on the model's predictions.

In summary, the SVM-DNN-RF algorithm offers superior prediction accuracy, robustness, and flexibility compared to other machine learning approaches, making it particularly effective for modeling the complex and nonlinear dynamic behaviors of composite structures in engineering applications.

5.1. Mathematics formulation of the mentioned algorithm

The formulation of the SVM-DNN-RF hybrid algorithm to predict the nonlinear dynamic behavior of composite structures integrates the principles and methodologies of Support Vector Machines (SVM), Deep Neural Networks (DNN), and Random Forest (RF) into a cohesive model. Each of these components contributes to the overall performance by addressing different aspects of the prediction task, such as handling non-linearity, feature selection, and improving generalization. Below is a high-level outline of the algorithm formulation:

1. SVM Component:

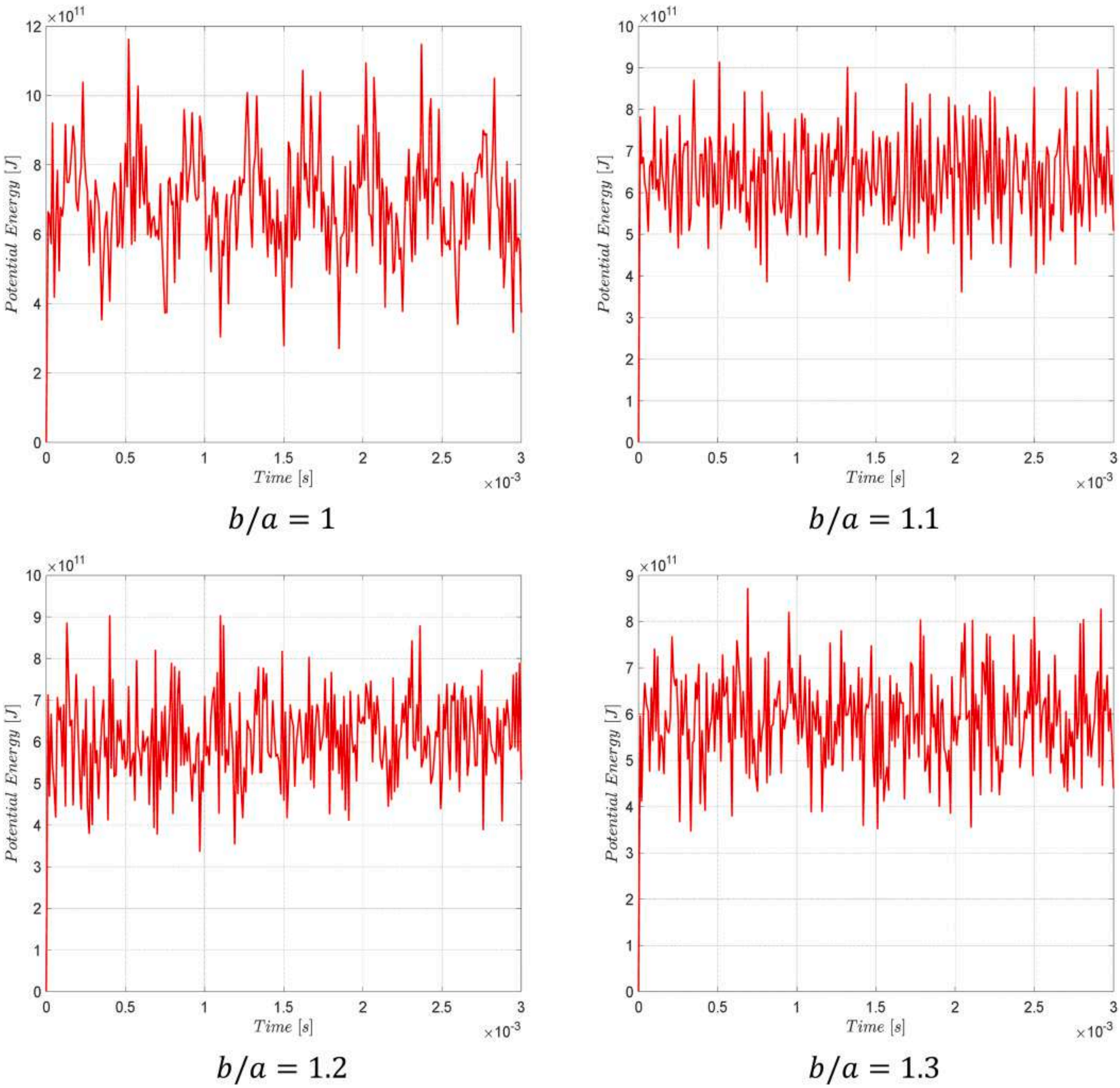

Fig. 11. Potential energy of the FG-TPMSM curved panel under excitation frequency for various b/a ratios.

SVM is used to classify or regress the data in a high-dimensional feature space, making it ideal for problems with complex, nonlinear relationships. The SVM algorithm can be formulated as:

$$\min\left(\frac{1}{2}\parallel w\|^2 + C\sum_{i=1}^{N}\xi_i\right), \tag{42}$$

Subject to:

$$y_i(w.x_i + b) \geq 1 - \xi_i,\ \xi_i \geq 0,\ i = 1, 2, \ldots, N \tag{43}$$

Where:

w: is the weight vector.

b: is the bias term.

ξ_i: are the slack variables that allow for some misclassification.

C: is a regularization parameter that controls the trade-off between maximizing the margin and minimizing classification error.

x_i: are the input features, and y_i are the corresponding labels (target variables). The nonlinear kernel function $K(x, x')$ is often used in practice to map the data into a higher-dimensional space, allowing for the capture of complex relationships.

2. DNN Component:

The DNN component is designed to capture deep, nonlinear patterns and interactions in the data. The general formulation for a feedforward neural network with one hidden layer can be written as:

$$y = f(W_2.g(W_1.X + b_1) + b_2). \tag{44}$$

Where:

X: is the input data matrix (composite structure features).

W_1 and W_2: are the weight matrices for the input and hidden layers, respectively.

b_1, and b_2: are the bias terms.

$g(.)$: is the activation function (such as ReLU, Sigmoid, or Tanh).

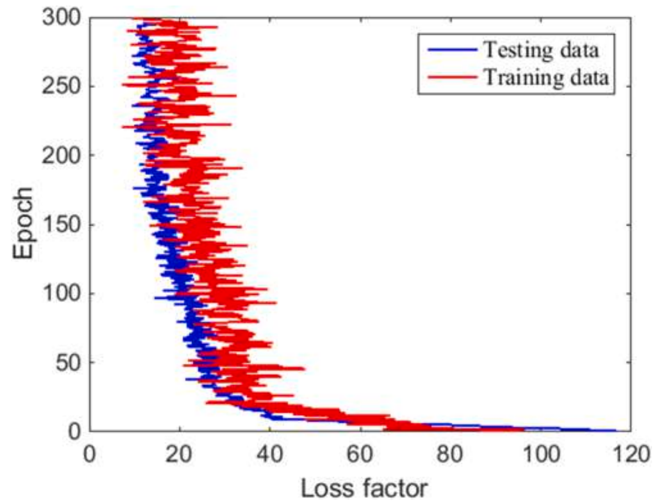

Fig. 12. Loss factor against epoch for presented SVM-DNN-RF algorithm.

$f(.)$: is the output activation function.

y: is the predicted output (e.g., nonlinear dynamic response).

The objective of training the DNN is to minimize the loss function (such as Mean Squared Error for regression tasks or Cross-Entropy for classification tasks), commonly expressed as:

$$L(y, \widehat{y}) = \frac{1}{N}\sum_{i=1}^{N}(\widehat{y}_i - y_i)^2. \tag{45}$$

Where $\widehat{y}$ are the predicted values and L is the loss function.

3. RF Component:

Random Forest is an ensemble learning method that builds multiple decision trees to predict the target value, improving prediction accuracy and robustness by averaging the outputs of individual trees. The RF algorithm can be defined as:

$$\widehat{y} = \frac{1}{T}\sum_{t=1}^{T} f_t(X). \tag{46}$$

Where:

T: is the number of trees in the forest.

f_t: is the prediction made by the $t-th$ decision tree.

X: is the input feature vector (composite structure data).

Each decision tree is trained by randomly selecting a subset of the features and samples from the dataset. The prediction is averaged across all trees to reduce overfitting and variance, providing a more robust estimate.

4. Hybrid SVM-DNN-RF Algorithm

The hybrid SVM-DNN-RF algorithm combines the strengths of each individual model into a unified framework. The general workflow involves the following steps:

1. Data Preprocessing: Collect and preprocess data from simulations of composite structures, which may include dynamic responses, material properties, and boundary conditions.

2. Training Phase:

SVM: Train the SVM component on the dataset to capture the nonlinear boundaries in the feature space.

DNN: Train the DNN component to learn deep patterns and relationships between the input features and dynamic responses.

RF: Train the Random Forest component by constructing multiple decision trees using random subsets of features and data points.

3. Prediction Phase: For a new set of input features X_{test}, the predictions from all three models are combined. The final prediction is typically made by averaging the outputs of each model:

$$\widehat{y}_{final} = \alpha.\widehat{y}_{SVM} + \beta.\widehat{y}_{DNN} + \gamma.\widehat{y}_{RF}. \tag{47}$$

Where:

$\widehat{y}_{SVM}$, $\widehat{y}_{DNN}$, and $\widehat{y}_{RF}$ are the predictions from the SVM, DNN, and RF models, respectively.

α, β, and γ are weights or coefficients assigned to each model, based on their individual performance or contribution.

4. **Model Evaluation**: The hybrid model is evaluated using standard metrics such as Mean Squared Error (MSE), Root Mean Squared Error (RMSE), or R-squared to assess its prediction accuracy.

5.2. Advantages of the hybrid formulation

Combining strengths: The combination of SVM's ability to handle high-dimensional non-linear data, DNN's capacity to learn deep features, and RF's ensemble learning approach provides a more accurate and robust model.

Handling complex behaviors: The algorithm effectively captures the nonlinear dynamics of composite materials under various conditions, which is difficult for simpler models to address.

Generalization: The ensemble approach helps prevent overfitting and improves the generalization of the model, making it more reliable for unseen data.

This hybrid formulation allows the SVM-DNN-RF algorithm to predict the nonlinear dynamic information of composite structures with high accuracy and efficiency, even for complex and large datasets generated from mathematical simulations.

6. Result and discussion

6.1. Validation

Fig. 3 presents a comparison of the time-history response of functionally graded graphene platelets reinforced composite (FG-GPLRC) plate subjected to a time-varying force, $q(t) = 2000\sin(450t)$. The data from the present study, shown in a red line, is compared with reference results from a previous study (Ref. [40]), indicated by black circular markers. The graph illustrates oscillations in the displacement response, measured in meters, over a time range of 0 to 0.1 s. The close alignment of the red curve with the black markers suggests strong agreement between the current study's results and the reference data, validating the present model's accuracy. The plate's material composition includes uniformly distributed graphene platelets (GPL-UD) with a weight percentage of 0.3%. Geometric parameters include an aspect ratio of $a/h = 20$ and plate dimensions $a = b$, where a and b are the plate's length and width, respectively. The applied force frequency of 450 rad/s induces high-frequency vibrations, captured in the waveform, demonstrating the model's ability to simulate the dynamic response of FG-GPLRC structures accurately. This validation supports the applicability of the present study's methodology for analyzing the vibrational behavior of FG-GPLRC plates.

6.2. Parametric result

Fig. 4 compares the dynamic deflection responses of a TPMS (triply periodic minimal surface) doubly curved panel under frequency excitation using different TPMS models. Subfigures (a), (b), and (c) display time-history plots under varying excitation frequencies and amplitudes, indicated as $q(t) = q_0\, sin(\Omega \times t)$, with unique parameter values q_0 and Ω for each case. Each subfigure includes curves from multiple TPMS models (PA1, PB1, and Gyroid types), shown in different colors. These comparisons reveal the influence of the TPMS model on the panel's deflection behavior under identical loading conditions. Variations in amplitude and phase across the models reflect differences in their structural properties, which impact the panel's dynamic response. In all cases, the TPMS model selection significantly affects the frequency and amplitude of deflection, with distinct response patterns in each subfigure. This analysis demonstrates the importance of TPMS model choice

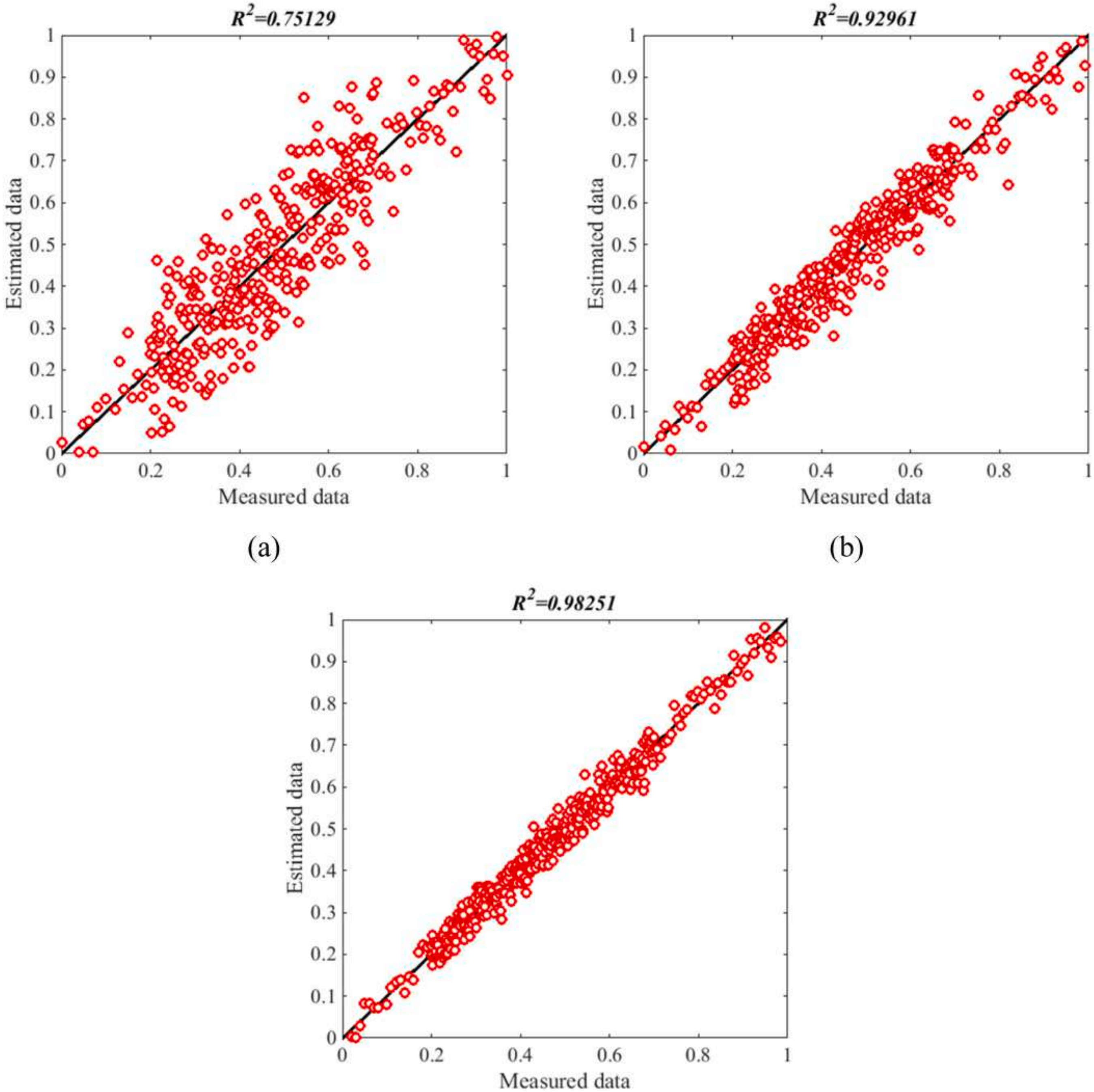

Fig. 13. Scatter plots comparing measured data with estimated data for three different models or scenarios, each labeled with an R^2 value.

Table 2
Comparing the dynamic deflection of the SVM-DNN-RF algorithm with the mathematics simulation results by varying the b/a, and $R_{\mathscr{X}}/a$.

b/a	$R_{\mathscr{X}}/a$			
	10		20	
	Mathematics	SVM-DNN-RF	Mathematics	SVM-DNN-RF
3	0.026039	0.026027	0.02979	0.029766
10	0.045315	0.044758	0.049864	0.049598
20	0.051195	0.051207	0.055551	0.054728

in optimizing dynamic performance under vibrational loads for doubly curved structures.

Fig. 5 illustrates the influence of different types of Triply Periodic Minimal Surfaces (TPMS) on the dynamic deflection behavior of a TPMS-based doubly curved panel under frequency excitation. The three subfigures (a), (b), and (c) correspond to different TPMS types: (a) TPMS of type P (Primitive), (b) TPMS of type D (Diamond), and (c) TPMS of type G (Gyroid). Each graph shows the panel's deflection over time under an excitation $q(t) = q_0\cos(\Omega \times t)$, where Ω is the excitation frequency. The deflections, depicted by different colors for various parameter values, illustrate how each TPMS structure responds dynamically under identical conditions. The waveforms indicate that the TPMS type significantly affects the amplitude and phase of deflection, with each type displaying distinct dynamic behaviors. The Primitive TPMS type (a) shows moderate deflections, the Diamond type (b) exhibits a similar but slightly varied pattern, and the Gyroid type (c) has the highest and most complex deflection amplitude among the three. This variation suggests that TPMS topology can be a critical factor in tuning the vibration characteristics of such panels, potentially informing their design for applications requiring specific dynamic responses to vibrational forces.

Fig. 6 demonstrates the impact of different TPMS (Triply Periodic Minimal Surface) types on the dynamic behavior of a TPMS-based doubly curved panel subjected to frequency excitation. The figure consists of two parts: (a) a plot of deflection over time, and (b) a phase-space plot of $\mathscr{W}$ versus $\dot{\mathscr{W}}$ (the deflection and its time derivative), which illustrates the system's dynamic stability and oscillatory patterns. In (a), the deflection varies over time for three TPMS types, represented by different colors. Each type shows distinct oscillation amplitudes and phases, indicating how TPMS topology influences the time-dependent response of the panel to the external excitation force $q(t) = q_0\cos(\Omega \times t)$. The curves highlight the differences in amplitude and response patterns among the TPMS types. In (b), the phase-space plot shows closed-loop trajectories for each TPMS type, suggesting stable oscillatory behavior. The variation in trajectory shapes reflects the impact of TPMS structures on dynamic response characteristics. This phase-space analysis helps reveal the influence of TPMS type on the stability and energy dissipation properties of the doubly curved panel under vibrational excitation, aiding in the design optimization for dynamic applications.

Fig. 7 explores the effect of different radius of curvature factors on the dynamic response of a TPMS (Triply Periodic Minimal Surface) doubly curved panel under frequency excitation. The figure includes two plots: (a) the deflection over time, and (b) the phase-space plot of $\mathscr{W}$ versus $\dot{\mathscr{W}}$ (deflection versus its time derivative). The analysis uses a Gyroid-type TPMS with varying radius of curvature ratios. In (a), the time-deflection plot presents the panel's deflection under an excitation force $q(t) = q_0\cos(\Omega \times t)$ with different curvature ratios. The curves in black, red, and blue represent curvature ratios of 10, 15, and 20, respectively, showing that an increase in curvature ratio affects both the amplitude and frequency of oscillations. Higher curvature ratios generally lead to increased deflection amplitude, indicating enhanced sensitivity to the excitation force. In (b), the phase-space plot shows the closed-loop trajectories for each curvature ratio, illustrating stable oscillations and dynamic behavior influenced by curvature variations. The larger curvature ratio (in blue) results in a wider trajectory, indicating higher energy absorption and more pronounced oscillations. This analysis reveals that adjusting the curvature ratio can effectively tailor the dynamic response of TPMS panels, which is essential for applications involving specific vibration and stability requirements.

Fig. 8 illustrates the impact of different b/a ratios on the dynamic behavior of a TPMS doubly curved panel, under a specific frequency excitation pattern. Subfigure (a) presents time-domain responses of $\mathscr{W}$ (displacement in the transverse direction) versus time for three different b/a ratios. The plot indicates varying amplitude and frequency of oscillations in $\mathscr{W}$, suggesting that changes in the b/a ratio significantly influence the panel's dynamic response. The black, red, and blue curves represent responses for distinct b/a ratios, with noticeable variations in oscillatory behavior, implying that each ratio has a unique influence on the panel's stiffness and natural frequency. Subfigure (b) displays phase-space plots showing the relationship between displacement and velocity for the same b/a ratios. The intricate closed-loop patterns indicate complex oscillatory behavior with nonlinear characteristics, where each curve's shape varies with the b/a ratio, demonstrating distinct response behaviors under periodic excitations. The figure as a whole highlights how tuning the b/a ratio affects the panel's vibrational characteristics, which could be crucial in designing TPMS structures for specific resonance or damping applications in engineering contexts.

Fig. 9 demonstrates the effect of various b/a ratios on the dynamic response of a TPMS doubly curved panel, specifically under a second frequency excitation pattern. In subfigure (a), the time-domain plot illustrates the transverse displacement over time for different b/a ratios. The distinct curves (black, red, and blue) represent these ratios, showing significant differences in oscillatory amplitudes and frequencies. Compared to the first excitation pattern (Fig. 8), this second pattern induces more complex, higher-frequency oscillations, indicating a shift in response behavior likely due to the altered excitation form, $q(t) = q_0\cos(0.6\omega \times t)$. Subfigure (b) presents the phase-space plots of displacement versus velocity for these ratios. The loops in the phase plot are denser and more intricate than in Fig. 8, indicating a more chaotic or complex response. The variation in shapes for each b/a ratio suggests that modifying the panel's geometric ratio significantly affects its stability and nonlinear dynamic characteristics under this second excitation form. Overall, this figure emphasizes how different excitation patterns and b/a ratios influence the panel's vibrational dynamics, relevant for structural control and optimization.

Fig. 10 shows the impact of varying excitation frequencies on the dynamic responses of a TPMS doubly curved panel, specifically looking at $\mathscr{W}$ (transverse displacement) versus *Time* (time), $\mathscr{W}$ versus $\dot{\mathscr{W}}$ (velocity), and $\dot{\mathscr{W}}$ versus $\mathscr{W}$ responses. Subfigure (a) presents the $\mathscr{W} - \mathit{Time}$ response, indicating how different excitation frequencies influence the time-domain oscillations. The overlapping curves (black, red, and blue) reflect the panel's response under distinct frequency conditions. Differences in amplitude and oscillatory patterns reveal the panel's sensitivity to frequency changes, affecting the system's stability and energy dissipation. Subfigures (b) and (c) illustrate phase-space plots, specifically the $\mathscr{W} - \dot{\mathscr{W}}$ and $\ddot{\mathscr{W}} - \mathscr{W}$ trajectories, respectively. In both, the looped patterns show how the system's dynamics change under various excitation frequencies. These intricate trajectories indicate nonlinear behavior, with each frequency producing unique loop structures. The denser and more complex patterns in (c) suggest a strong dependence on excitation frequency, with higher frequencies amplifying the complexity of response trajectories. Overall, this figure highlights how tuning excitation frequency influences the dynamic characteristics of the TPMS panel, which is essential for engineering applications requiring specific resonance, stability, and damping behavior.

The Fig. 11 presents the potential energy response of a curved panel under excitation, evaluated for different aspect ratios ($b/a = 1$, 1.1, 1.2, and 1.3). Each subplot corresponds to a distinct aspect ratio, with potential energy plotted on the y-axis (in joules) and time on the x-axis (in seconds). The observed variations in potential energy for different b/a ratios illustrate the influence of panel geometry on energy response under dynamic excitation. As the b/a ratio increases from 1 to 1.3, fluctuations in potential energy persist, but with varying amplitude and frequency characteristics. These trends suggest that the structural response of the curved panel is sensitive to changes in aspect ratio, impacting its energy storage and dissipation under loading. Such analysis aids in understanding the dynamic behavior of these advanced materials in engineering applications.

6.3. Results of presented SVM-DNN-RF algorithm

As mentioned before, the SVM-DNN-RF algorithm combines Support Vector Machines, Deep Neural Networks, and Random Forests to predict nonlinear dynamic responses in composite structures. By leveraging simulation-based datasets, this hybrid model enhances predictive accuracy, capturing complex patterns and relationships in dynamic structural behavior, crucial for advanced engineering applications. Fig. 12 illustrates the performance of the proposed SVM-DNN-RF algorithm, where the "Loss factor" is plotted against the "Epochs" for both training and testing datasets. The "Epoch" represents each iteration of training, while the "Loss factor" indicates the algorithm's error rate or how far the predicted values deviate from actual outcomes during each epoch. In this graph, two sets of curves are presented: the red curve represents the loss factor for the training data, while the blue curve represents the loss factor for the testing data. Both curves demonstrate a similar trend; they start with high loss factors at the beginning (close to 100 on the x-axis) and decrease rapidly as epochs progress. This reduction in loss factor suggests that the algorithm is learning effectively and improving its accuracy over successive epochs.

As the number of epochs increases, the loss factors for both training and testing data converge towards zero, indicating that the model is achieving better predictive accuracy and minimizing errors over time. The high density of points in the early epochs reflects rapid learning, as the model quickly reduces errors, while the gradual convergence in later epochs indicates a more refined, stabilized learning.

The relatively close alignment between training and testing loss factors suggests good generalization performance, meaning the algorithm is not overfitting to the training data and performs consistently on new, unseen data. This convergence demonstrates the efficacy of the SVM-DNN-RF algorithm in achieving high predictive accuracy with minimal error across both datasets.

Fig. 13 shows scatter plots comparing measured data with estimated data for three different models or scenarios, each labeled with an R^2 value that represents the coefficient of determination, a metric indicating the goodness of fit. The closer the R^2 value is to 1, the more accurately the estimated data matches the measured data, signifying a better model performance. Fig (13.a) shows a moderate correlation between the measured and estimated data, with some visible deviations from the ideal 45-degree line. An R^2 value of 0.75129 indicates that approximately 75% of the variance in the measured data is explained by the model. Although the points generally trend along the line, there is noticeable scatter, suggesting that the model's predictions are not entirely accurate. In Fig (13.b), the fit between measured and estimated data improves substantially, with an R^2 value of 0.92961. The points are much closer to the line, indicating a high level of accuracy. This suggests that around 93% of the variability in the measured data is accounted for by the model, indicating a strong predictive performance and a significant improvement over the previous model. Fig (13.c) shows the highest R^2 value of 0.98251, indicating an excellent fit between the estimated and measured data. The points are tightly clustered around the 45-degree line, meaning that the model explains approximately 98% of the variance in the measured data. This high correlation demonstrates that this model or approach provides the most accurate predictions among the three. Overall, these plots demonstrate progressive improvement in the predictive accuracy of the models or algorithms, with each successive model achieving a higher R^2 value and closer alignment between measured and estimated data.

A summary of key parameters in the presented SVM-DNN-RF algorithm are presented as follows to correctly simulate a similar problem to the presented one:

- **SVM**: kernel='rbf', C = 1.0, epsilon=0.1, gamma='scale'.
- **DNN**: hidden_layers= [64,32], activation='relu', loss='mse', optimizer='adam', epochs=50, batch_size=10.
- **RF**: n_estimators=100, max_depth=10, min_samples_split=2, min_samples_leaf=1, max_features='sqrt'.
- **Model Combination**: Weights like 0.3 for SVM and RF, 0.4 for DNN

Via the mentioned parameters, Table 2 compares the dynamic deflection values predicted by the SVM-DNN-RF algorithm with those from mathematical simulations under varying b/a and $R_{\mathscr{X}}/a$ ratios. Results show a high degree of agreement between the algorithm and mathematical values across all configurations, demonstrating the model's accuracy. For instance, at $b/a = 3$ and $R_{\mathscr{X}}/a = 10$, deflection values from both methods are nearly identical, indicating reliable predictive performance. Slight discrepancies appear as the ratios increase, but overall, the SVM-DNN-RF algorithm effectively approximates theoretical results, supporting its robustness for dynamic deflection predictions.

7. Conclusion

This study provided a comprehensive nonlinear dynamic analysis of functionally-graded TPMS double-curved panels, examining the influence of structural parameters and excitation frequencies on their vibrational behavior. Through time-domain and phase-space analysis, it was observed that variations in the b/a ratio and excitation frequency significantly impacted the transverse displacement and velocity responses of FG-TPMS panels. These variations led to complex oscillatory patterns and nonlinear phase trajectories, underscoring the high sensitivity of FG-TPMS structures to both design and operational parameters. The findings offered valuable insights into the intricate dynamic responses of these advanced materials, supporting their optimization for applications that demand high strength-to-weight ratios, resonance control, and effective damping. In addition, the study introduced a novel SVM-DNN-RF algorithm, integrating SVM, DNN, and RF methods to accurately predict nonlinear dynamic behaviors. This hybrid model leveraged the classification accuracy of SVM, the deep feature extraction capabilities of DNN, and the robustness of RF to achieve enhanced predictive performance, especially in capturing complex nonlinear relationships within mathematically simulated datasets. Results showed that the SVM-DNN-RF algorithm outperformed standalone models in predicting the dynamic behaviors of FG-TPMS panels, offering a reliable and precise tool for dynamic analysis. Together, these findings contribute to the advancement of FG-TPMS panel design by providing a predictive framework for dynamic responses and a deeper understanding of the parameters influencing these behaviors. This work has practical implications for engineering fields requiring lightweight, durable materials with optimized dynamic properties, including structural engineering, aerospace, and complex system modeling.

This research explores the nonlinear dynamics of FG-TPMS panels, although it is important to note that these geometries are still very straightforward. High-complexity intelligent structures need to be researched to guarantee that the effort is worthwhile. The linear vibration study solely considers the linear strain components of the structures. In contrast to huge amplitude, however, nonlinear vibration provides a more complete picture of the structures' nonlinear dynamic behavior. Future research into the absorbed energy capacity and nonlinear dynamics of the structure under rain or air flow pressure is, thus, a promising area of inquiry.

CRediT authorship contribution statement

Shaoyong Han: Investigation, Resources, Software, Validation, Visualization, Writing – review & editing. **Zhen Wang:** Writing – review & editing, Writing – original draft, Visualization, Validation, Supervision, Software, Resources, Investigation. **Mohammed El-Meligy:** Investigation, Resources, Software, Validation, Writing – review & editing. **Khalid A. Alnowibet:** Investigation, Resources, Software, Writing – review & editing.

Declaration of competing interest

We declare that we do not have any commercial or associative interest that represents a conflict of interest in connection with the work submitted.

Funding

The Talents Subsidized Project (R23165) of Tongling University under Grant 2024tlxyrc020. The research project (K24061) of Tongling University under Grant 2024tlxyxdz280. The authors extend their appreciation to King Saud University, Saudi Arabia for funding this work through Researchers Supporting Project number (RSP2024R305), King Saud University, Riyadh, Saudi Arabia.

Data availability

Data will be made available on request.

References

[1] M. Nebab, M. Dahmane, A. Belqassim, H.A. Atmane, F. Bernard, M. Benadouda, R. Bennai, L. Hadji, Fundamental frequencies of cracked FGM beams with influence of porosity and Winkler/Pasternak/Kerr foundation support using a new quasi-3D HSDT, Mech. Adv. Mater. Struc. (2023) 1–13.
[2] L. Ould Larbi, M. Saad, N. Zouatnia, L. Hadji, A.S. Sayyad, A simple refined plate theory for buckling problems of in-plane bi-directional functionally graded plates with porosity under various boundary conditions, Mech. Adv. Mater. Struc. (2024) 1–10.
[3] R. Mohammadi, M. Hosseini, Modeling and free vibration analysis of a rotating functionally graded thin-walled hub-blade system under aerothermoelastic loading, Aerosp. Sci. Technol. 146 (2024) 108935.
[4] M. Javani, M.R. Eslami, Y. Kiani, Active control of thermally induced vibrations of temperature-dependent FGM circular plate with piezoelectric sensor/actuator layers, Aerosp. Sci. Technol. 146 (2024) 108997.
[5] N. Latroch, M. Dahmane, A.S. Benosman, R. Bennai, H.A. Atmane, M. Benadouda, Inclined crack identification in bidirectional FG beams on an elastic foundation using the h-version of the finite element method, Mech. Adv. Mater. Struc. (2023) 1–7.
[6] Z. Sadoun, R. Bennai, M. Nebab, M. Dahmane, H.A. Atmane, Investigation of the behavior of an RC beam strengthened by external bonding of a porous P-FGM and E-FGM plate in terms of interface stresses, Struc. Monitor. Maint. 10 (2023) 315–337.
[7] S. Debbaghi, M. Dahmane, M. Benadouda, H.A. Atmane, N. Bendenia, L. Hadji, Wave propagation of bi-directional porous FG beams using Touratier's higher-order shear deformation beam theory, Coup. Sys. Mech. 13 (2024) 43.
[8] N. Zouatnia, L. Hadji, H.A. Atmane, M. Nebab, R. Madan, R. Bennai, M. Dahmane, Analysis of free vibration in bi-directional power law-based FG beams employing RSD theory, Coup. Syst. Mech. 13 (2024) 359.
[9] M. Mouheb, A. Fellah, M.A. Khorchef, M.R. Larbaoui, K. Boualem, Impact of using FGM materials for improving the efficiency of an internal combustion engine, Acta Mech. Slovaca 28 (2024).
[10] N. Zouatnia, L. Hadji, H.A. Atmane, L.O. Larbi, Impact of porosity distribution and grading parameters on free vibration of functionally graded beams, Stud. Eng. Exact Sci. 5 (2024) e6945.
[11] M. Yaghoobi, M. Sedaghatjo, M. Karkon, L. Hadji, Free vibration analysis of pores functionally graded plates using new element based on Hellinger–Reissner functional, Steel Compos. Struc. 49 (2023) 713.
[12] Q. Wu, N. Chen, M. Yao, Y. Niu, C. Wang, Nonlinear dynamic analysis of FG fluid conveying micropipes with initial imperfections, Int. J. Struc. Stabil. Dyn. (2024) 2550017.
[13] T. Fu, X. Hu, C. Yang, Impact response analysis of stiffened sandwich functionally graded porous materials doubly-curved shell with re-entrant honeycomb auxetic core, Appl. Math. Model. 124 (2023) 553–575.
[14] K. Liu, S. Zong, Y. Li, Z. Wang, Z. Hu, Z. Wang, Structural response of the U-type corrugated core sandwich panel used in ship structures under the lateral quasi-static compression load, Marine Struc. 84 (2022) 103198.
[15] H. Nguyen-Xuan, K.Q. Tran, C.H. Thai, J. Lee, Modelling of functionally graded triply periodic minimal surface (FG-TPMS) plates, Compos. Struct. 315 (2023) 116981, https://doi.org/10.1016/j.compstruct.2023.116981.
[16] Q. Zhang, Q. Xu, M.A. El-Meligy, M. Tlija, On the dynamics of improved perovskite solar cells: introducing SVM-DNN-GA algorithm to predict dynamical information, Aerosp. Sci. Technol. 154 (2024) 109478.
[17] N.V. Nguyen, K.Q. Tran, P. Phung-Van, J. Lee, H. Nguyen-Xuan, An isogeometric analysis of functionally graded triply periodic minimal surface microplates, Aerosp. Sci. Technol. 137 (2023) 108270.
[18] S. Zhang, D. Da, Y. Wang, TPMS-infill MMC-based topology optimization considering overlapped component property, Int. J. Mech. Sci. 235 (2022) 107713.
[19] G. Altintas, Vibration properties of TPMS based structures, Int.. J. Scient. Technol. Res. 4 (2018) 27–42.
[20] N. Novak, O. Al-Ketan, L. Krstulović-Opara, R. Rowshan, R.K.A. Al-Rub, M. Vesenjak, Z. Ren, Quasi-static and dynamic compressive behaviour of sheet TPMS cellular structures, Compos. Struct. 266 (2021) 113801.
[21] Y.-W. Zhang, G.-L. She, M. Eltaher, Nonlinear transient response of graphene platelets reinforced metal foams annular plate considering rotating motion and initial geometric imperfection, Aerosp. Sci. Technol. 142 (2023) 108693.
[22] H.-X. Ding, M. Eltaher, G.-L. She, Nonlinear low-velocity impact of graphene platelets reinforced metal foams cylindrical shell: effect of spinning motion and initial geometric imperfections, Aerosp. Sci. Technol. 140 (2023) 108435.
[23] L.-L. Gan, G.-L. She, Nonlinear transient response of magneto-electro-elastic cylindrical shells with initial geometric imperfection, Appl. Math. Model. 132 (2024) 166–186.
[24] M. Al-Furjan, M. Habibi, D. won Jung, G. Chen, M. Safarpour, H. Safarpour, Chaotic responses and nonlinear dynamics of the graphene nanoplatelets reinforced doubly-curved panel, Europ. J. Mech-A/Solids 85 (2021) 104091.
[25] W. Zhang, H. Zheng, T. Liu, Y. Zheng, Y. Qian, Nonlinear resonant responses and chaotic dynamics of three-dimensional braided composite cylindrical shell, Aerosp. Sci. Technol. (2024) 109099.
[26] C.-L. Qiao, H.-Y. Xu, Z.-Y. Ye, Sensitivity and uncertainty analysis of the nonlinear flight dynamics system of the flexible body, Aerosp. Sci. Technol. 139 (2023) 108389.
[27] L. Boni, M. Bassetto, A.A. Quarta, G. Mengali, Nonlinear dynamics of flexible heliogyro subject to sinusoidal root pitch command, Aerosp. Sci. Technol. 130 (2022) 107920.
[28] J. Shi, B. Zhao, J. He, X. Lu, The optimization design for the journal-thrust couple bearing surface texture based on particle swarm algorithm, Tribol. Int. (2024) 109874.
[29] Y. Wang, O. Sigmund, Topology optimization of multi-material active structures to reduce energy consumption and carbon footprint, Struc.. Multidiscipl. Optimiz. 67 (2024) 5.
[30] R. Chen, B. Zhao, Q. Xin, X. Niu, Z. Xie, X. Lu, D. Zou, Analysis of transient lubrication and wear coupling behaviors considering thermal effect and journal misalignment for main bearings under dynamic load, Wear 554 (2024) 205478.
[31] Y. Wang, O. Sigmund, Multi-material topology optimization for maximizing structural stability under thermo-mechanical loading, Comput. Methods Appl. Mech. Eng. 407 (2023) 115938.
[32] W. Zhang, J. Lin, Y. Huang, B. Lin, S. Kang, Temperature-dependent debonding behavior of adhesively bonded CFRP-UHPC interface, Compos. Struct. 340 (2024) 118200.
[33] G. Feng, S. Li, L. Xiao, W. Song, Mechanical properties and deformation behavior of functionally graded TPMS structures under static and dynamic loading, Int. J. Impact. Eng. 176 (2023) 104554.
[34] D.T. Dong, T.Q. Minh, B.T. Tu, K.Q. Tran, H. Nguyen-Xuan, Nonlinear thermo-mechanical static stability analysis of FG-TPMS shallow spherical shells, Thin-Wall. Struc. (2024) 112343, https://doi.org/10.1016/j.tws.2024.112343.
[35] N.V. Nguyen, K.Q. Tran, J. Lee, H. Nguyen-Xuan, Nonlocal strain gradient-based isogeometric analysis of graphene platelets-reinforced functionally graded triply periodic minimal surface nanoplates, Appl. Math. Comput. 466 (2024) 128461.
[36] L.J. Gibson, Cellular solids, Mrs Bulletin 28 (2003) 270–274.
[37] J.N. Reddy, Theory and Analysis of Elastic Plates and Shells, CRC press, 2006.
[38] H. Huang, C. Xue, W. Zhang, M. Guo, Torsion design of CFRP-CFST columns using a data-driven optimization approach, Eng. Struct. 251 (2022) 113479.
[39] Qian Zhang, et al., Active control vibrations of aircraft wings under dynamic loading: Introducing PSO-GWO algorithm to predict dynamical information, Aerosp. Sci. Technol. 153 (2024) 109430.APA.
[40] P.H. Cong, N.D. Duc, New approach to investigate the nonlinear dynamic response and vibration of a functionally graded multilayer graphene nanocomposite plate on a viscoelastic Pasternak medium in a thermal environment, Acta Mech. 229 (2018) 3651–3670.